

Characterization of the Microstructure and Mechanical Behavior of Intact and Damaged Alumina

by

Calvin Lo

A thesis submitted in partial fulfillment of the requirements for the degree of

Master of Science

Department of Mechanical Engineering

University of Alberta

© Calvin Lo, 2020

Abstract

Advanced ceramics such as alumina serve a critical role as a structural material in many applications (e.g., light-weight turbine blades, ultrasonic cutting, and body armor). To improve their performance in these applications, it is important to understand how microstructural features affect the mechanical response of ceramics under loading. X-ray computed tomography (XCT) is well-suited to characterizing the microstructure of advanced ceramics since it can non-destructively visualize micron-scale internal features. By coupling XCT characterization to mechanical testing, this thesis aims to investigate the effects of processing induced pores and internal cracks on the material behavior of intact and damaged alumina.

In the first part of this thesis, XCT characterization is combined with uniaxial compression experiments to study intact alumina, where the major processing-induced defects are pores. Quantitative XCT measurements of pores in AD85 alumina showed low variability across a range of pore characteristics, with median pore size values ranging from $16.0\ \mu\text{m}$ to $17.2\ \mu\text{m}$ over ten samples. In terms of spatial distribution, analytic comparison against randomly distributed points showed that the spacing between pores was highly regular. Voronoi tessellation showed that while spacing is mostly independent of pore size, smaller pores exhibited greater variability in spacing. Mechanical testing results were found to vary depending on strain rate, with greater scatter at quasi-static rates than dynamic strain rates. The coefficient of variation for compressive strength and failure strain decreased from 10.28% and 10.23%

at quasi-static to 5.20% and 4.17% at dynamic rates. Based on the low scatter in general pore characteristics between the 10 samples, the differences in variability between quasi-static and dynamic properties are attributed to variability in testing conditions (e.g. misalignment of platens) and the activation of a greater number of pores in dynamic compression.

In the second part of this thesis, a similar approach was used to study the behavior of pre-damaged alumina. XCT was used to characterize internal crack networks in pre-damaged alumina, focusing on crack characteristics such as surface area and crack orientation. Quasi-static and dynamic compression experiments showed that crack damage led to a reduced stiffness and rate of lateral expansion during the early stages of loading. With further compression, elastic properties were found to increase towards intact levels. Shortly before failure, the crack growth was found to increase the lateral strain rate and reduce the stiffness. Digital image correlation (DIC) coupled with high-speed imaging was used to observe the localized deformation mechanisms activated during loading, including lateral crack closure, axial crack opening and closing, and inclined crack sliding. The dynamic compressive strength of the damaged alumina decreased with increasing crack surface area, however, quasi-static strength results did not differ significantly between intact and damaged specimens. In-situ visualization of the dynamic compression experiments revealed that the damaged specimens exhibited a mixed fracture mode that included axial splitting and failure along pre-existing cracks.

In summary, this thesis presents: 1. Improved characterization of microstructural defects through XCT for the design, manufacturing, and modeling of advanced ceramics; and 2. Insights into the evolution of mechanical properties, deformation mechanisms, and fracture behavior of damaged ceramics.

Preface

Chapter 2 of this thesis has been published in *Materials Characterization* as C. Lo, T. Sano, and J.D. Hogan, “Microstructural and Mechanical Characterization of Variability in Porous Advanced Ceramics using X-ray Computed Tomography and Digital Image Correlation”. I was responsible for performing the experiments and analysis in this study as well as the manuscript composition. T. Sano contributed to manuscript edits. J.D. Hogan was the supervisory author and was involved with concept formation and manuscript composition.

Chapter 3 of this thesis has been published in *Journal of the European Ceramic Society* as C. Lo, T. Sano, and J.D. Hogan, “Deformation Mechanisms and Evolution of Mechanical Properties in Damaged Advanced Ceramics”. I was responsible for performing the experiments and analysis in this study as well as the manuscript composition. T. Sano contributed to manuscript edits. J.D. Hogan was the supervisory author and was involved with concept formation and manuscript composition.

Acknowledgements

First I would like to thank my supervisor, Dr. James Hogan, for his encouragement and mentorship throughout my graduate degree. I am truly grateful for the trust he has placed in me and for all of the great opportunities he has provided for personal growth. I could not have asked for a better supervisor.

Next I would like to acknowledge my CDAM lab mates for their helpful discussions, feedback, and support. I would like to thank Haoyang Li for the many ways he has helped me throughout my degree. From waking me up in class to helping me set up experiments, he has been a great collaborator and friend these past two years. I would like to thank Kapil Bhagavathula for his generous help in countless experiments. I would like to thank Brendan Koch for sharing his insightful perspective on my research in our many discussions. I have enjoyed sharing this journey with all of you, and I wish you all continued success.

I wish to thank Ning Zhu and Sergei Gasilov from the Canadian Light Source for their help in generating X-ray computed tomography scans. Here I want to express my gratitude to all who traveled with me to the Canadian Light Source and spent sleepless nights performing experiments (Pouyan Motamedi, Kapil Bhagavathula, Brendan Koch, Haoyang Li, and Benhour Amirian). I also want to thank Bernie Faulkner and Rick Bubenko from the Mechanical Engineering machine shop for sharing their expertise and help in conducting experiments. I would like to acknowledge the US Army Research Laboratory and the Natural Sciences and Engineering Research Council of Canada for their funding in my graduate degree.

Finally, I want to thank Felicia Truong for her encouragement and belief in me through the ups and downs these past six years.

Contents

1	Introduction	1
1.1	Motivation	1
1.2	Thesis Objectives	2
1.3	Thesis Goals	2
1.4	Contributions	3
1.5	Thesis Structure	3
2	Microstructural and Mechanical Characterization of Variability in Porous Advanced Ceramics using X-ray Computed Tomography and Digital Image Correlation	5
2.1	Introduction	7
2.2	Experimental Method	8
2.2.1	Material	8
2.2.2	X-ray Computed Tomography Analysis	9
2.2.3	Mechanical Testing	18
2.3	Experimental Results	20
2.3.1	Pore Size Distribution	20
2.3.2	Pore Morphology	22
2.3.3	Microstructural Anisotropy	22
2.3.4	Spatial Distribution of Pores	24
2.3.5	Mechanical Testing	25
2.4	Discussion	29
2.4.1	Manufacturing	30
2.4.2	Parameters for Computational Models	31
2.4.3	Variability in Microstructure and Properties	32
2.5	Conclusion	34
2.6	Acknowledgment	35
3	Deformation Mechanisms and Evolution of Mechanical Properties in Damaged Advanced Ceramics	36
3.1	Introduction	38
3.2	Experimental Method	40
3.2.1	Material and Specimen Preparation	40
3.2.2	X-ray Computed Tomography	41
3.2.3	Mechanical Testing	45
3.3	Results	48
3.3.1	Crack Orientation and Surface Area	48
3.3.2	Quasi-static and Dynamic Compression Experiments	48
3.3.3	Localized Deformation in Damaged Ceramics	53
3.3.4	Failure Process of Damaged Ceramics	57
3.4	Discussion	59

3.4.1	Relationship Between Crack Orientation and Crack Closure	59
3.4.2	Relationship Between Crack Surface Area and Strength	61
3.4.3	Ballistic Performance of Damaged Ceramics	64
3.4.4	Computational Models for Ballistic Impacts	65
3.5	Conclusion	66
3.6	Acknowledgment	66
4	Concluding Remarks	68
4.1	Implications	68
4.2	Future Work	69
	References	71
	Appendix A Background: Split-Hopkinson Pressure Bar	83

List of Tables

2.1	Material properties for AD85 alumina as reported by CoorsTek Inc.	9
2.2	Summary of stiffness, strength, and failure strain in quasi-static (QS) and dynamic (DYN) compression experiments with coefficient of variation (COV)	29

List of Figures

2.1	A) AD85 alumina sample dimensions with hot pressing direction along the long edge. B) Speckled sample under dynamic compression experiment lighting taken using the Shimadzu HPV-X2.	10
2.2	Schematic of reconstruction process showing A) XCT scan of AD85 at 3 μm ; B) binary cross-sections of segmented pores; C) 3D rendering of reconstructed defects.	11
2.3	Cumulative distribution function plot of the major axis length for all 10 AD85 samples.	21
2.4	A) Examples of the limiting cases for AD85 pore shapes that can be presented using general ellipsoids. B) Intermediate axis length plotted against minor axis length. Both lengths are normalized by the major axis. Color bar shows normalized density.	23
2.5	A) Spherical coordinate convention for orientation. B) AD85 nearest neighbor orientation polar histogram. C) AD85 pore major axis orientation polar histogram. The blue and orange represent the ϕ and θ distributions, respectively. The black line at 90° represents the long dimension of the sample.	24
2.6	Log-log plot of Voronoi cell volume as a function of pore major axis length in AD85. Contour shows normalized density. Dashed lines indicate boundaries to the high frequency band where the majority of data points lie. The inset is a visualization of Voronoi tessellation where the red dots are seed points.	26
2.7	Strain profiles from DIC are matched up to the stress profile computed from the transmitted gauge. The inset shows the area of interest (AOI) each strain profile is computed from. The red strain profile is the average of the entire face.	27
2.8	Stress-strain curves for the quasi-static (solid line) and dynamic (dashed line) compression experiments of AD85 alumina.	28
3.1	(A) XCT scan of AD995 alumina. Due to the high resolution of the scan, small features are difficult to observe under low magnification. A magnified view of the center of the specimen is included on the right to show the internal crack. (B) 3D reconstruction of internal crack network showing the extent and inter-connectedness of the crack network. The red box outlines the boundary of the scan volume.	41
3.2	Stacked bar graph showing the crack surface area for each damaged specimen (D1 to D4). The quasi-static tests are denoted by QS and the dynamic tests are denoted by DYN. The divisions denote the area contribution of crack faces with different orientations to the loading axis.	49

3.3	Stress-strain and lateral-axial strain curves for intact and damaged specimens tested under (A) quasi-static and (B) dynamic compression. The quasi-static tests are denoted by QS and the dynamic tests are denoted by DYN. Intact tests are represented using dashed lines and denoted by IN while the damaged tests are represented using solid lines and denoted by D. The lateral-axial strain curves for QS D1, DYN D2, and DYN D4 are shown separately in insets so the evolution of the other curves are not dwarfed by the large lateral strains.	50
3.4	(A) Lateral contour plot of QS D1 showing the opening of a large axial crack. (B) Lateral contour plot of QS D3 showing a large axial crack that accommodates the expansion of adjacent solid material. (C) XCT scan of QS D4 cropped and filtered to show the crack network on the surface of the specimen. This image is overlaid with surface contours for QS D4 from (D) to (F) to show the location of localized strains in reference to the crack. (D) Axial contour plot of QS D4 showing localized compressive strains at lateral and low-angled inclined cracks. (E) Lateral contour plot of QS D4 showing the closing of axial and high-angled inclined cracks under compression. (F) Shear contour plot of QS D4 showing shear strains along inclined cracks. The white arrows are included to show relative motion of the crack surfaces.	54
3.5	(A) XCT scan of QS D4 showing the regions where axial and shear strains are queried. The regions of interest include (1 and 2) intact solid material, (3) an axial crack, (4 and 5) inclined cracks, (6) a triple junction, and (7) a lateral crack. (B) The evolution of axial strain at the regions of interest over time. (C) Shear strain development as a function of axial strain for each region of interest.	56
3.6	Stress-time histories of dynamic compression of intact (shown in black) and pre-damaged (shown in red) AD995 with high-speed video images showing failure process. Red arrows are used to indicate surface crack initiation points.	58
3.7	Transition strain plotted as a function of the crack surface area for orientations between 0° and 60° for each specimen. Blue points represent quasi-static results and red points represent dynamic results.	61
3.8	Compressive strength is plotted as a function of total crack surface area. Blue points represent quasi-static results and red points represent dynamic results. Diamonds indicate intact results and circles indicate damaged results.	62
A.1	Split-Hopkinson pressure bar setup: The incident and transmitted bars are shown in the foreground. The dynamic experiments were visualized using the Shimadzu HPV-X2 camera with the K2 DistaMax infinity lens and the REL Inc LED array ring light.	84

Chapter 1

Introduction

1.1 Motivation

Advanced ceramics are light-weight structural materials that are ideal for protection against ballistic threats because of their low density, high hardness, and high strength. In particular, alumina (Al_2O_3) was one of the first advanced ceramics to be employed in personnel protection systems during the Vietnam War due to its wide availability and low cost[1], and it continues to be widely utilized in composite body armors today. Acting as the strike face material in personnel armor systems, alumina is subjected to high rates of deformation and complex stress-states, which ultimately lead to fracture and fragmentation during an impact event[2]. Consequently, extensive research has been focused on understanding the dynamic behavior of alumina and other advanced ceramics with the goal of improving ballistic performance[3–5]. To this end, a range of laboratory-based experiments (e.g., split-Hopkinson pressure bar) have been developed to probe the mechanical response of advanced ceramics under well-defined loading conditions. In recent years, advancements in high-speed imaging and image processing have made it possible for these experiments to be visualized in-situ and characterized with greater depth. Alongside experimental studies, material models have also been developed to incorporate relevant physics and predict the dynamic response of advanced ceramics[6–8]. Central to these efforts are microstructural characterization studies[9, 10], which facilitate investigations into the physical mechanisms responsible for the observed mechanical behavior and contribute critical microstructural parameters

for computational models. To further our understanding of the factors that govern the performance of ceramics, it is important to improve and integrate material characterization and testing techniques.

1.2 Thesis Objectives

The objective of this thesis is to investigate the effects of microstructural features, namely defects and cracks, on the mechanical behavior of aluminum oxide. X-ray computed tomography (XCT) is used to characterize the microstructure of intact and damaged aluminum oxide, focusing on quantitative measurements for internal pores and cracks. Following microstructural characterization, in-situ high-speed imaging is combined with uniaxial compression experiments to explore the mechanical response of alumina. The microstructural and mechanical characterization data generated in this thesis are then linked to gain insights into structure-property relationships for intact and damaged alumina.

1.3 Thesis Goals

The goals of this thesis are summarized as follows:

1. Develop an analysis framework for quantitative characterization of internal pores and cracks from XCT scans of intact and damaged alumina. Emphasis is placed on utilizing the three-dimensional information accessible through XCT in this analysis. For intact alumina, the characteristics of interest include pore size, shape, orientation, and spatial distribution. For damaged alumina, the characteristics of interest include crack surface area, volume, and surface orientation.
2. Characterize the strength, stiffness, and failure strain of intact and damaged alumina at quasi-static and dynamic strain rates through uniaxial compression experiments coupled with high-speed photography.
3. Study the effects of pre-existing crack structures on the deformation of

alumina under uniaxial compression, focusing on the evolution of mechanical properties, localized strains, and fracture behavior.

4. Study the relationships between XCT measurements of microstructural features and the mechanical behavior of intact and damaged alumina.

1.4 Contributions

The contributions of this thesis are summarized as follows:

1. This thesis extends the scope of quantitative material characterization through XCT by introducing new characterization metrics for microstructural inhomogeneities and internal crack networks.
2. This thesis presents new microstructural and mechanical characterization data on intact and damaged alumina.
3. This thesis presents new insights into the effects of crack damage on material behavior.

1.5 Thesis Structure

This thesis is organized as follows:

- Chapter 1 introduces the motivation for studying aluminum oxide and outlines the thesis objective, thesis goals, contributions, and thesis structure.
- Chapter 2 details a study focused on the characterization of defect populations through XCT and the mechanical variability of intact alumina. This study, titled “Microstructural and Mechanical Characterization of Variability in Porous Advanced Ceramics using X-ray Computed Tomography and Digital Image Correlation”, was published in *Materials Characterization* in September 2019[11].

- Chapter 3 documents a study on the behavior of damaged alumina, in which XCT is applied to characterize internal cracks in pre-damaged alumina, and DIC is used to characterize the local deformation features caused by crack structures. This study, titled “Deformation Mechanisms and Evolution of Mechanical Properties in Damaged Advanced Ceramics”, was published in the *Journal of the European Ceramics Society* in February 2020 [12].
- Chapter 4 summarizes the outcomes and implications of this research and outlines directions for future work.
- Appendix A provides background on the split-Hopkinson pressure bar apparatus used for dynamic compression experiments in this thesis.

Chapter 2

Microstructural and Mechanical Characterization of Variability in Porous Advanced Ceramics using X-ray Computed Tomography and Digital Image Correlation

Calvin Lo^a, Tomoko Sano^b, James D. Hogan^a

^a*Department of Mechanical Engineering, University of Alberta, AB T6G 2R3, Canada*

^b*Weapons and materials Research Directorate, Army Research Laboratory, Aberdeen Proving Ground, MD 21005, USA*

Abstract

This paper explores microstructural and mechanical variability in porous ceramics, combining advanced X-ray computed tomography (XCT) and digital image correlation (DIC) techniques to characterize an alumina material. The results show low variability in microstructure, with median pore size values for this alumina ranging from 16.0 μm to 17.2 μm across ten samples. Spatial analysis showed internal pores are regularly distributed, and though spacing was found to be largely independent of pore size, the variability in spacing was shown to be greater for smaller pores. Mechanical results show a strain-rate dependence and greater scatter at quasi-static

rates, with the coefficient of variation for compressive strength and failure strain decreasing from 10.28% and 10.23% at quasi-static to 5.20% and 4.17% at dynamic rates. In view of the consistency demonstrated in the microstructure, the difference in variability between the quasi-static and dynamic mechanical properties is attributed to variability in testing conditions (e.g. misalignment of platens) and the activation of a greater number of pores in dynamic compression. In summary, these results motivate the use of new spatial characterization parameters via XCT for links to manufacturing, the integration of realistic microstructures into computational models, and focus on the role of defect distributions in dynamic compressive failure events.

Keywords: X-ray computed tomography microstructure digital image correlation defect variability

2.1 Introduction

Advanced ceramics commonly serve as critical structural components in body armor[4], tooling[13], and prosthetic[14] applications. To optimize the processing of advanced ceramics for these applications, it is important to consider the role of microstructural defects in the brittle failure process. Microstructural defects such as pores or secondary phase inclusions can arise due to incomplete densification or the use of excess sintering aids[15]. Under compressive loading, like in impact, these pre-existing defects serve as stress concentration sites[16], degrade bulk material properties[17], and have a significant influence on fragmentation behaviour[18]. Physics-based models have been developed to account for the effects of internal defects on the mechanical properties[19, 20] and dynamic failure[21–23] of brittle materials.

To accurately capture the effects of pre-existing flaws, defect characteristics are required as model inputs. However, while average defect size, volume fraction, and number density are common model inputs, parameters relating to defect orientation and spatial distribution have received limited consideration in theoretical and characterization studies. Furthermore, most single value characterization parameters are limited in that they do not account for the variability in defect characteristics. Owing to a lack of 3D characterization data in advanced ceramics, 3D models often rely on the use of data from 2D characterization studies, and microstructural inputs in computational models are frequently idealized in the absence of characterization data.

X-ray computed tomography (XCT) is well-suited for the 3D characterization of inhomogeneous microstructures in advanced ceramics. XCT is a visualization technique that relies on the contrasts in x-ray attenuation within a material to image internal features. Past defect characterization studies typically utilized optical or scanning electron microscopy to image microstructural features [24, 25]. However, microstructural flaws are distributed throughout the volume of the material, and traditional imaging techniques require either very thin samples or serial sectioning of the sample to observe internal flaws [26]. In addition, 2D characterization tools are limited in their ability to fully

capture the size or geometry of 3D features. In contrast, XCT can visualize internal features non-destructively and access 3D geometries. With the availability of current computed tomography systems, it is possible to resolve microstructural features on the scale of microns across scan volumes on the scale of cubic millimeters. As a result, there has been an increased focus on the use of XCT for the quantitative characterization of microstructures in a variety of materials in recent years (e.g., boron carbide [27], composites [28], and titanium alloys [29]).

With this in mind, this paper is motivated by the works of Li et al.[30, 31], whose efforts focused on methods for 3D characterization of inhomogeneous microstructure, and Graham-Brady[32], whose modeling work highlighted the effects of defect spatial distributions on the variability of the strength of materials. Building on the works of the motivating papers, this paper will explore the pore characteristics and mechanical behaviour of aluminum oxide (Al_2O_3), an advanced ceramic that has commonly been used in armor components. XCT was applied to characterize the pores, with a focus on improving methods for interpreting 3D data that can be generalized to future ceramic systems. Characterization parameters relating to pore size, morphology, orientation, and spatial distribution were evaluated to assess microstructural variability across multiple samples. Following pore characterization, compression experiments were performed at quasi-static and dynamic strain rates to determine the link between mechanical and microstructural variability. This paper will conclude by discussing the results in the context of manufacturing, computational model parameters, and rate-dependent failure mechanisms in brittle materials. The improved characterization techniques and mechanical results presented will advance the development of advanced ceramics.

2.2 Experimental Method

2.2.1 Material

XCT characterization and compression experiments were performed on AD85 alumina from CoorsTek Inc.(Vista, California, US)[33]. Table 2.1 shows

manufacturer values for AD85 material properties. Previous microstructural characterization performed by the authors on AD85 have shown that the dominant form of meso-scale defect in AD85 microstructure are isolated intergranular pores[34].

Table 2.1: Material properties for AD85 alumina as reported by CoorsTek Inc.[33]

Material	ρ (g/cm ³)	σ_c (GPa)	E (GPa)	ν
AD85 (Al_2O_3)	3.42	1.93	221	0.22

This material was selected because the pore sizes observed in AD85 are compatible with the resolution of the XCT scanner used for this study, and alumina is a common armor material. Figure 2.1A shows a schematic of the specimen, specifying the geometry and load direction. Ten cuboidal specimens measuring 2.3 mm by 2.7 mm by 3.5 mm in size were machined from different locations on multiple CoorsTek Inc. AD85 tiles. The small size of the specimen was chosen to accommodate the strength of the Kolsky bar used for dynamic compression, as well as the synchrotron x-ray source used for high resolution imaging. The cuboidal shape was chosen so that a flat sample surface could be visualized during compression experiments (as shown in Figure 2.1B) for 2D digital image correlation measurements, as will be discussed later in the Mechanical Testing section. The samples were cut from the tile with the long dimension of the sample parallel to the shortest dimension, or thickness, of the tile.

2.2.2 X-ray Computed Tomography Analysis

2.2.2.1 X-ray Computed Tomography Scans

Microstructural characterization was performed using X-ray computed tomography. All following microstructural analysis is performed using the digital reconstruction of defects visualized through XCT. XCT scans of the samples were carried out at the Biomedical Imaging and Therapy (BMIT) beamline at the Canadian Light Source synchrotron facility (Saskatoon, Saskatchewan, Canada). Synchrotron radiation is ideal for high resolution computed tomography due to its high intensity, which produces a high signal to noise ratio. The

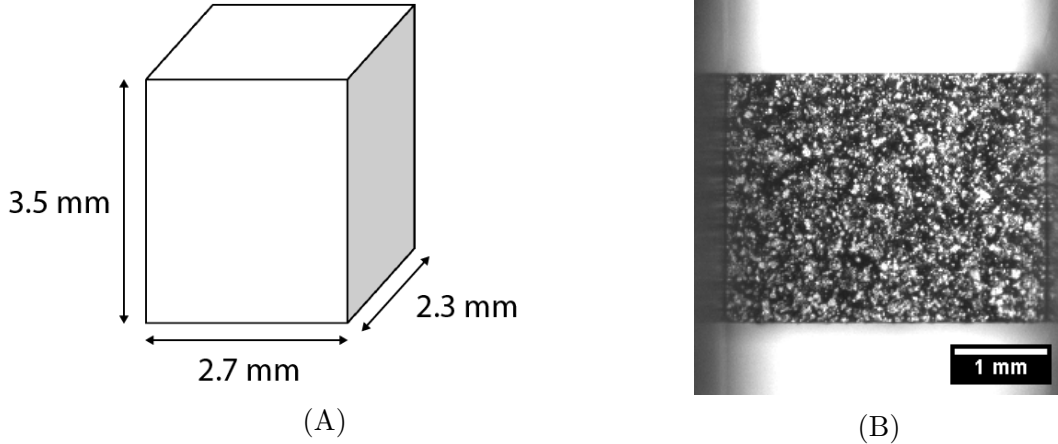


Figure 2.1: A) AD85 alumina sample dimensions with hot pressing direction along the long edge. B) Speckled sample under dynamic compression experiment lighting taken using the Shimadzu HPV-X2.

scans were carried out at the 05B1-1 POE-2 endstation[35] using a monochromatic beam. All images were captured using the ORCA-Flash 4.0 camera in conjunction with the Hamamatsu AA60 detector. For each specimen, 3001 projections were taken over 180° of rotation, and 799 tomograms were reconstructed. Each scan has a voxel size of $3\ \mu\text{m}$. Figure 2.2A shows a reconstructed cross-section of the AD85 microstructure in a representative scan (AD85 01). A low-pass Gaussian filter was applied to the sinograms to remove ring artifacts. Dark speckles in the scan represent pores while the gray area represents the alumina grains. Individual grains cannot be resolved at this scale. The scan volume was large enough to encompass the entire sample, however, edge effects distort features near the corners and edges of the specimen. To avoid the distorted regions, only the central volume consisting of a cylinder with a height of 2.1 mm and a diameter of 2.7 mm was considered for analysis of pore size, shape, and spatial distributions.

2.2.2.2 Image Segmentation and Filtering

All image segmentation and data analysis was performed on MATLAB (2018a, Natick, US). The first step of the analysis was to apply image segmentation to identify the pores in the XCT scans. The segmentation process divides pixels in the scans into foreground (1's) and background (0's) pixels,

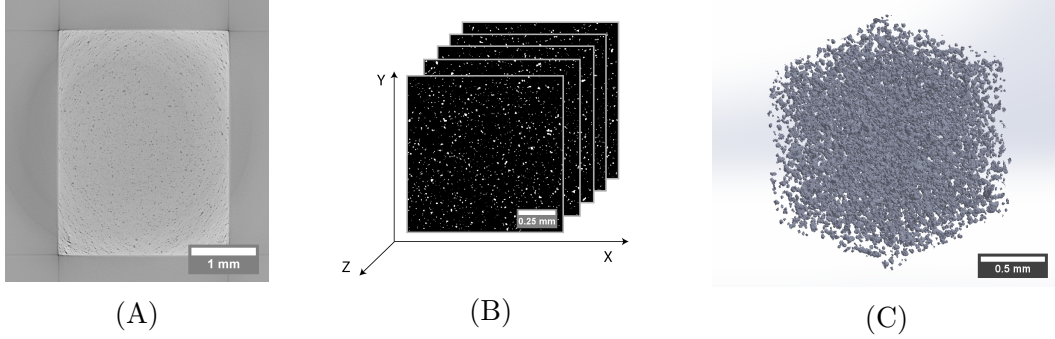


Figure 2.2: Schematic of reconstruction process showing A) XCT scan of AD85 at $3 \mu\text{m}$; B) binary cross-sections of segmented pores; C) 3D rendering of reconstructed defects.

generating binary images where foreground pixels represent pore area. Due to a difference in X-ray attenuation, the void in a pore will show up with a different range of grayscale values from the adjacent alumina grains. This contrast in grayscale values can be used to isolate pores, or any other discernible features, by grayscale thresholding. The choice of the grayscale threshold will affect the accuracy of the segmentation, and over-segmentation of pores in this step of the process can introduce noise into characterization results later. To minimize noise from possible over-segmentation, segmentation was performed using adaptive local thresholds. Unlike global thresholds, which are typically chosen based on the intensities of pixels in the entire image, locally adaptive thresholds are computed based on the mean intensity of pixels in the neighborhood of each pixel. Rather than dividing all pixels into foreground and background by a single global threshold, this method uses a local threshold for each pixel to make the determination between foreground and background. Segmentation by locally adaptive thresholds is more robust to scan artifacts and contrast changes than global thresholds because it takes into account local grayscale contrasts[36]. There is insufficient contrast in the XCT scans in this study to differentiate between the glassy phase from the alumina grains, so there is no risk of locally thresholding microstructural constituents other than pores. Figure 2.2B shows the binary segmented cross-sections, where the black background represents alumina grains and the white dots, the foreground, represents pores. The binary images resulting from segmentation were

then combined into a 3D matrix, and connected components analysis (using 26 connectivity) was performed to identify individual three-dimensional pores. Figure 2.2C shows a rendering of a set of 3D reconstructed pores, which is the culmination of the segmentation process and connected components analysis. The microstructural analysis in the following sections are carried out using these sets of digitally reconstructed pores.

Sampling limitations related to the voxel must be considered when performing analysis on XCT reconstructions. The voxel is the three-dimensional analog of the pixel, and it defines the smallest volume that can be represented digitally. However, this is not the same as the smallest *resolvable* volume. For every three-dimensional object reconstructed from XCT scans, pixels from multiple cross-sections must be combined to reconstruct the volume. Consequently, a lower limit on the number of voxels required to adequately represent a single object should be set to exclude from the analysis features that cannot be properly resolved. In addition, applying a minimum volume limit will eliminate noise generated from over-segmentation, which are typically small in size and randomly located in space. For these reasons, the total set of reconstructed pores for each specimen in this study were filtered by a minimum of 8 voxels, a resolution limit consistent with those used in the literature [29, 37, 38].

2.2.2.3 Ellipsoid Representation of Pores

In past optical microscopy and SEM characterization studies [24, 26], the *pore size* was typically defined as the equivalent diameter, which is the diameter of a circle with the same area as the observed pore. This idea can be extended to three dimensions and the equivalent diameter can be defined as the diameter of a sphere with the same volume as the reconstructed defect. However, this definition does not adequately characterize the length of non-spherical pores, where the span of the pore will differ depending on the direction. Furthermore, the characteristic length of interest in micro-mechanical models is often the longest length spanned by a general defect [39], which may be underestimated by this method. Defect morphology is also often

characterized by sphericity, which compares the ratio of the defect circumference to area, or surface area to volume in three-dimensions. Both characterization definitions essentially model defects as circles, or spheres in three-dimensions, but defects in ceramics can take on a variety of shapes. For instance, graphitic inclusions in boron carbide have been found to be disk-like in three-dimensions[18], and Carniglia[19] has commented that intergranular pores in polycrystalline ceramics typically have moderate to high aspect ratios. For these types of defects, a spherical definition will not accurately capture the defect size or shape. This is an important consideration as theoretical works have shown that the pore shape has a significant effect on the macroscopic compliance[40, 41], and past investigators have emphasized the importance of incorporating pore geometry when modeling the effects of porosity on mechanical properties[19, 42].

Based on qualitative assessments of the XCT scans and digital reconstructions in this study, the majority of pores in AD85 alumina are closed, non-overlapping, and have a convex shape. The reconstructed pores are therefore well-suited to ellipsoidal representation. To fit an ellipsoid to the reconstructed pore, we compute the co-variance matrix of the (x,y,z) coordinates of the voxels that make up the reconstructed pore. The eigenvalues of the co-variance matrix represent the principal axis lengths of the fitted ellipsoid, and the eigenvectors represent the orientation of the principal axes. In the equation for a general ellipsoid,

$$\frac{x_0^2}{a^2} + \frac{y_0^2}{b^2} + \frac{z_0^2}{c^2} = 1 \quad (2.1)$$

where x_0 , y_0 , and z_0 are the local coordinate axes for the ellipsoid, the principal major semi-axis lengths, in decreasing order, are defined as a , b , and c . Note the local coordinate axes for the ellipsoid are distinguished from the global coordinate axes used in the general XCT analysis because the ellipsoid may be oriented such that the principal axes are not aligned with the global coordinate system. Using a fitted ellipsoid, the characteristic length of the pore would then be defined as the major axis length, defined as $2a$. This definition is more

flexible for determining the characteristic length of flaws that are not spherical in shape.

In addition, the ratio of the principal axis lengths provide information on the *shape* of the flaw. For instance, if the major axis length is much larger than the minor and intermediate axis lengths ($a \gg b \approx c$) then the pore shape is needle-like (example shown later in Figure 2.4A when discussing shape results). It is important to note that the digital representation of pores by discrete cubic voxels can bias the morphology of the reconstructed pore, especially when the pore is resolved by a small number of voxels. When the pore size is similar to the voxel size, the pore shape cannot be adequately represented. Therefore, a volume cut-off of 125 voxels was used in this paper to filter pores for morphology analysis to ensure only resolvable pore morphologies are included in the analysis. This limit is consistent with those used in the literature [29, 38]. Note that the methods in this paper were developed for convex pores or inclusions, which may be reasonably approximated by ellipsoidal representation. Failure in other materials may be controlled by defects at different scales (e.g. dislocations[43] or stacking faults[44]), which currently cannot be imaged using XCT, or defects of different morphologies (e.g. closed cracks), which require different representations, and so the methods in this paper may not be transferable to those systems.

2.2.2.4 Microstructural Anisotropy

Anisotropy in the microstructure has been shown to develop in sintered ceramics[45–47], and it can have an effect on anisotropy in mechanical properties[48]. Microstructural anisotropy can arise from preferred directionality in the (i) pore *orientation* and (ii) *spatial distribution* of pores. The first type of anisotropy refers to the orientation of *individual* pores, and it can be characterized by the orientation of the major axis of the fitted ellipsoid. Preferred directionality in pore orientation can be detected by examining the distribution of major axis orientation for all pores. The second type of anisotropy refers to banded dispersions, in which pores exhibit tighter spacing in a specific direction[49, 50]. This type of anisotropy can be identified by examining the

angle between nearest neighbor pores. The orientation between nearest neighbors is characterized by the vector that joins the centroids of nearest neighbor pores. For a set of pores that are isotropically distributed, all angles should be equally likely, but certain angles are expected to dominate for banded or aligned dispersions. Using these methods, anisotropy in the microstructure can be quantified through XCT and linked to mechanical property anisotropy.

2.2.2.5 Spatial Distribution of Pores

The study of the spatial distribution of defects, including investigating the nearest neighbor spacing between defects, is motivated by the role of inter-defect spacings on fragmentation[16, 18], strain-rate dependency[51, 52], and strength[32] in advanced ceramics. Characterization of spatial distributions may also shed light on the formation of process-induced defects and links to manufacturing parameters. The spatial distribution of defects is commonly characterized by scalar metrics such as number density or volume fraction. Defect density can be quantified through XCT reconstructions by taking the number of defects identified through connected components analysis and dividing by the total reconstructed voxel volume. Volume fraction, or in this case, porosity, can be quantified by considering the ratio of foreground voxels, which represent pore volume, to the total number of voxels, which represent the total sample volume. However, these scalar metrics do not provide any information on the type of spatial distribution observed, nor do they account for local variations in spacing. For example, while a random distribution of defects may share the same global density as a clustered distribution, local defect density will differ dramatically.

Such fluctuations in defect spacing have been linked to an increased variability in compressive strength in brittle materials[32], as well as a greater dependence on porosity for strength and stiffness[53]. Ultimately, density is an indirect and limited measure of defect spacing. With access to the spatial coordinates of individual defects through XCT reconstructions, deeper spatial analysis is possible. This section will outline nearest neighbor and tessellation methods for analyzing spatial relationships.

Nearest neighbor distance distributions have been used to classify the type of spatial distribution observed in inhomogeneous microstructures[50, 54, 55]. This classification is based on comparisons between the observed nearest neighbor distribution and that of a Poisson process. Using reconstructed XCT data, the observed nearest neighbor distance between pores can be computed by taking the distance between the centroidal coordinates of a pore and its nearest neighbor. The Poisson process models a randomly located distribution of points in which the location of each point is independent of the locations of all other points. Two ratios are used to classify the observed distribution:

$$Q = \frac{\bar{r}}{E(\bar{r})} \quad (2.2)$$

$$R = \frac{s^2}{E(s^2)} \quad (2.3)$$

where \bar{r} and s^2 are the mean and variance of the nearest neighbor distance for the observed pores, and $E(\bar{r})$ and $E(s^2)$ are the expected mean and variance of the nearest neighbor distance for the Poisson process. Physically, the Q and R ratios quantify the deviation of the observed nearest neighbor spacing from that of a random distribution. To obtain the expected mean and variance in nearest neighbor distance for a three-dimensional Poisson process for comparison, the following analytical expressions have been developed [30, 50, 54]:

$$E(\bar{r}) = 0.893 \left(\frac{3V}{4\pi N} \right)^{\frac{1}{3}} \quad (2.4)$$

$$E(s^2) = 0.105 \left(\frac{4V}{3\pi N} \right)^{\frac{2}{3}} \quad (2.5)$$

where N is the number of points and V is the volume of the region of interest. The following guidelines for interpreting the two ratios have been given by Bansal and Ardell[55] as:

$Q \approx 1, R \approx 1$: random distribution

$Q > 1, R \ll 1$: regular distribution

$Q < 1, R < 1$: clustered distribution

$Q < 1, R > 1$: clusters in a random background distribution

Note that the Poisson distribution models points while the observed defects have finite volume. As the size and volume fraction of the defects increase, the defect spacing will naturally deviate from that of a point distribution. Therefore, the above criteria are only valid for small pores with volume fractions less than 5% [55]. The pores in alumina under analysis in this paper were found to have volume fractions of approximately $4.1 \pm 0.1\%$ on average, so the comparison is valid. The data that is generated through this analysis will be used to characterize the global defect distribution pattern in AD85 alumina. For materials where the secondary phase particles are present in higher volume fractions, the spacing comparison can be made against randomly simulated microstructures with the same size distribution, like in Yang et al.[56].

Local spatial characteristics in AD85 microstructure can be analyzed through Voronoi tessellation. Voronoi tessellation has been used to analyze spatial distributions in many applications, including astronomy[57], biology[58], and ecology[59]. In terms of material science, Voronoi tessellation has been applied to investigate the spatial distributions of particle reinforcements in composites[54, 56] and defects in metals[30, 31, 50]. Given a set of points in a volume, Voronoi tessellation is a method for discretizing the volume into polyhedrons, where the geometry of the polyhedrons are determined based on the distances between points. Each discretized polyhedron, known as a Voronoi cell, envelopes one point. The faces of the cell are made up of planes bisecting the shortest lines between adjacent points such that each cell contains the space that is closest to its associated point than any other point. To apply this method using XCT data, the centroids of the reconstructed pores can be used as seed points for generating a tessellation. The geometry of the cells also define unique near neighbors for each pore; cells sharing faces are counted as near neighbors, and each pore is therefore surrounded by a finite set of uniquely defined neighbors. The strength of this method is that it extracts spatial information for each individual pore, including cell volume, local volume fraction (ratio of pore volume to cell volume), mean near neighbor distance, and num-

ber of near neighbors. As a result of each pore being associated with a cell, spatial properties of the Voronoi cell can be linked to the characteristics of the individual pore, such as size, shape, or orientation.

2.2.3 Mechanical Testing

Quasi-static uniaxial compression experiments were performed using a Material Testing System (MTS) 810 load frame. The specimens were compressed along the longest dimension (3.5 mm). Loading was carried out using displacement control at a constant rate of 3.5×10^{-3} mm/s, which corresponds to a nominal strain rate of 1×10^{-3} s⁻¹. However the actual strain rate is approximately an order of magnitude lower owing to the compliance of the load frame, and this is known for these experiments because digital image correlation was used to explore strain in the sample (methods presented later). Due to the high hardness of alumina, the specimens can indent into the load frame's compression platens under loading, leading to a non-uniform stress distribution. To prevent indentation and provide a hard surface for uniform stress distribution, tungsten carbide platens jacketed in titanium were inserted between the specimen and the load frame's compression platens. The specimen and tungsten carbide platen interfaces were lubricated with high-pressure grease to allow for free lateral expansion during loading. A Promon U750 high speed camera capturing 630 by 750 pixels at 100 frames per second (FPS) was used to visualize the sample surface during the quasi-static compression experiments.

Dynamic compression experiments were performed on a Kolsky bar apparatus. The incident and transmitted bars were made of maraging steel with a stiffness of 200 GPa and a density of 8100 kg/m³. All bars were 12.7 mm in diameter. Again, tungsten carbide platens jacketed in titanium were used to protect the bars from indentation, and specimen-platen interfaces were lubricated with high pressure grease to allow for free lateral expansion. Note that the tungsten carbide platens are impedance matched to the incident and transmitted bars to minimize wave reflections at interfaces. The triangular incident pulse was created using a cylindrical maraging steel striker 304 mm

in length in conjunction with a tin pulse shaper measuring 3.175 mm in diameter and 1 mm in thickness. This provided a rise time of 230 μs and we found that good stress-equilibrium was obtained in our specimens (discussed later in Figure 2.7). The surface of the specimen was visualized using a Shimadzu HPV-X2 ultra-high-speed camera recording at 500,000 FPS with a 1000 ns exposure time. In total, 128 frames spanning 400 x 250 pixels were captured for each experiment. At these frame rates, we were able to capture failure and post-peak fragmentation process.

Digital image correlation (DIC) was applied to in-situ recordings of experiments to obtain deformation measurements on specimens in quasi-static and dynamic compression experiments. DIC is a computer vision method that tracks speckle patterns on surfaces to compute deformation fields. The two-dimensional DIC technique is well established and has been applied to study the behaviour of a variety of materials (e.g., composites[60], aluminum foams[61], and mild steels[9]). See Pan et al.[62] and Dong et al.[63] for discussions on DIC theory and experimental design. Due to the small size of the specimens in this study, it was challenging to produce a speckle pattern suitable for DIC measurements. Conventional methods such as commercial spray can paints or rollers produce speckles that are too coarse for samples of this size. An airbrush with a 0.15 mm nozzle set capable of producing speckles with diameters on the order of microns was found to generate a sufficiently fine speckle pattern (i.e. 5-10 pixels per speckle). One of the challenges to capturing at high frame rates, as required for capturing the dynamic experiments in this study, is producing adequate illumination on the specimen surface for low exposure times. To increase the reflectivity of the specimen surface, high gloss metallic paint was used to create the speckle pattern (see Figure 2.1B). In addition, a ring light consisting of a high power LED array from REL Inc. was used to provide increased illumination on the specimen surface. DIC analysis was performed using the commercial software VIC-2D (v6 2018) from Correlated Solutions (Irmo, South Carolina, US). The region of interest was discretized into 27 x 27 pixel subsets with a step size of 7 pixels. Correlation analysis was carried out using the zero-normalized sum of

squared differences correlation criterion and the optimized 8-tap interpolation scheme[64]. Strains were computed from the displacement fields using the engineering strain tensor. The computed strain histories were matched to the stress histories to produce stress-strain curves. Quasi-static stress information was obtained from the load cell in the MTS load frame. Dynamic stress information was obtained using the transmitted bar strain gauge signal using:

$$\sigma(t) = E \frac{A_0}{A_B} \epsilon_T(t) \quad (2.6)$$

where σ is the stress (Pa) in the specimen, t is time (s), E is the Young's Modulus (Pa) of the transmitted bar, A_0 is the specimen cross-sectional area (m^2), A_B is the transmitted bar area (m^2), and $\epsilon_T(t)$ is the strain from the transmitted gauge.

2.3 Experimental Results

2.3.1 Pore Size Distribution

First we begin by presenting the pore size distribution in AD85 alumina. Shown in Figure 2.3 is the cumulative distribution of the pore size for 10 samples that eventually were tested in both quasi-static and dynamic compression experiments. For a given major axis length, the cumulative distribution defines the probability that the pore size is less than or equal to that major axis length. In this study, the cumulative distribution was computed empirically using:

$$F(l) = \frac{1}{n} \sum_{i=1}^n I(l_i \leq l) \quad (2.7)$$

where l is the major axis length, l_i is the total distribution of major axis lengths, n is the total number of pores, and $F(l)$ is the empirical cumulative distribution function, which approximates the true cumulative distribution function for large n . The function I has a value of 1 when $l_i \leq l$, and 0 otherwise. Used in combination with the summation, I indicates the number

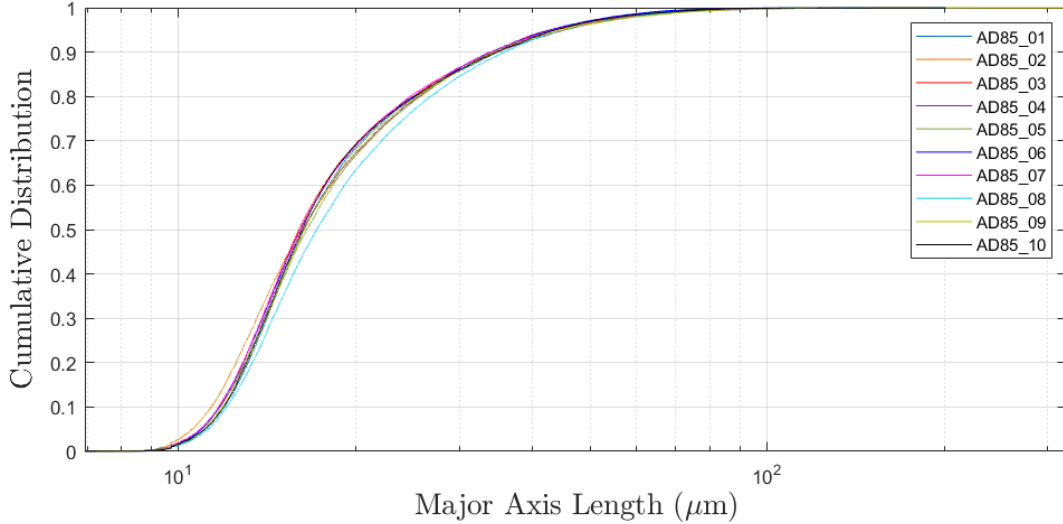


Figure 2.3: Cumulative distribution function plot of the major axis length for all 10 AD85 samples.

of pores with a major axis length less than l . In total, there are between 16,540 and 19,091 pores reconstructed for each sample in this study.

The large number of pores quantified in this study is a key advantage of XCT analysis when compared the 565[65] or 1000[24] pores that are characterized through SEM or optical microscopy in other alumina studies. Given the large number of pores observed, the empirical cumulative distribution function is a good approximation of the theoretical distribution. From Figure 2.3, we observe that the pore size distribution remains mostly constant across all 10 samples, with median (50th percentile) values ranging from $16.0\ \mu\text{m}$ to $17.2\ \mu\text{m}$. In all cases, pores smaller than $36.5\ \mu\text{m}$ represent more than 90% of the defect population. Beyond $70\ \mu\text{m}$, the distribution ends in a long tail, indicating reduced frequency for larger defects. The largest pores in each sample range from 148 to $367\ \mu\text{m}$, which are 10-25 times larger than the median pore size. The distribution is therefore dominated by smaller pores, and large pores are infrequent. Overall, the pore size distribution is well controlled in AD85 alumina, especially considering that the samples come from different locations across multiple tiles.

2.3.2 Pore Morphology

To characterize pore morphology, we analyze the principal axis lengths of the fitted ellipsoids. The intermediate axis lengths of the fitted ellipsoids are plotted against the corresponding minor axis lengths for sample AD85 01 in Figure 2.4B. These results are similar for other samples considered in this study. Both lengths are normalized by the major axis length. The contour represents normalized frequency, with warmer colors representing higher frequency and cooler colors representing lower frequency. The ratios of the two normalized lengths serve as useful descriptors of the shape of the ellipsoid. Points that fall on the diagonal line are pores with equal intermediate and minor axis lengths. Therefore, the upper right corner characterizes spherical pores ($a=b=c$), and the bottom left corner characterizes high aspect ratio, needle-like pores ($a \gg b \approx c$). Flat disc-like pores, in which the major and intermediate axes are much longer than the minor axis ($a \approx b \gg c$), are represented by the upper left corner of the plot. In the pore data set for AD85, few data points occupy this region of the plot, so the pores tend to be rounded rather than flat. All of the above limiting cases are shown schematically in Figure 2.4A. The wide spread of the points in Figure 2.4B indicates that the pores can take on a wide range of shapes, while the concentration of points near the center shows that there is a preferred shape for the pores. Based on the location of the high frequency region, the majority of pores are slightly prolate spheroids. To give a quantitative measure of the general pore shape, the center values of the normalized intermediate and minor axis lengths in the high frequency region are (0.73, 0.62) in Figure 2.4B. This trend is observed consistently as the center normalized intermediate and minor axis lengths are 0.75 ± 0.04 and 0.64 ± 0.05 for all ten samples.

2.3.3 Microstructural Anisotropy

The orientation between nearest neighbors and the angles of individual pores were examined to identify anisotropy in the microstructure. Orientation in 3D is described using the two angles θ and ϕ (see Figure 2.5A for orien-

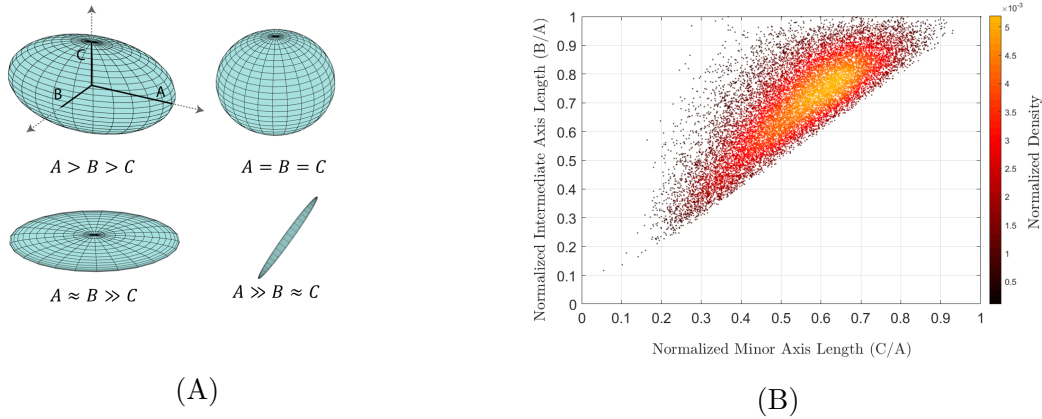


Figure 2.4: A) Examples of the limiting cases for AD85 pore shapes that can be presented using general ellipsoids. B) Intermediate axis length plotted against minor axis length. Both lengths are normalized by the major axis. Color bar shows normalized density.

tation definition). The orientation between nearest neighbors is shown in a normalized polar histogram in Figure 2.5B. To show only unique angles, the θ distribution was collapsed to between 0° and 180° . The solid black line at 90° in the θ plane indicates the direction of the long dimension of specimen, which is parallel to the thickness of the tile from which the specimen is cut. Both the θ and ϕ distributions span the whole range of possible angles, showing that near neighbors can take on a variety of orientations. In the ϕ distribution, the frequency for most angular bins are between 1.7% and 2.4% of the total distribution, with no distinct preference amongst the angles for higher or lower frequencies. In the θ distribution, the majority of the angular bins that are less than 60° and greater than 120° exhibit frequencies at or below 2%, while angular bins between 60° and 120° consistently show frequencies above 2%. For a set of randomly distributed pores, all orientations between nearest neighbors should be equally likely. Therefore, it is expected that one third of the nearest neighbor pairs would have an orientation between 60° and 120° , however, 38.5% of the pores were found to have a θ angle between 60° and 120° . In terms of spacing, this shows that there is an increased frequency in nearest neighbors along the thickness of the tile. This preference is observed consistently in all 10 samples, which suggests that the anisotropy in spatial distribution is global

in AD85 alumina. Because the exact manufacturing process for this material is not known, it is difficult to identify the cause of this anisotropy. However, based on comparisons of ultra-sonic characterization data in the literature, Chang et al.[66] have theorized that uniaxial forming processes, such as hot pressing, cold pressing, extrusion, or pressure casting, can induce anisotropic pore distributions in which the pore density is greater along the pressing direction. Other characterization studies have linked anisotropic grain growth in alumina to uniaxial pressure when elongated powder particles are used[45, 46], though none have directly characterized the pores. Ultimately, this anisotropy is expected to have little effect on the mechanical behaviour of the material, as the deviation from an isotropic distribution is small.

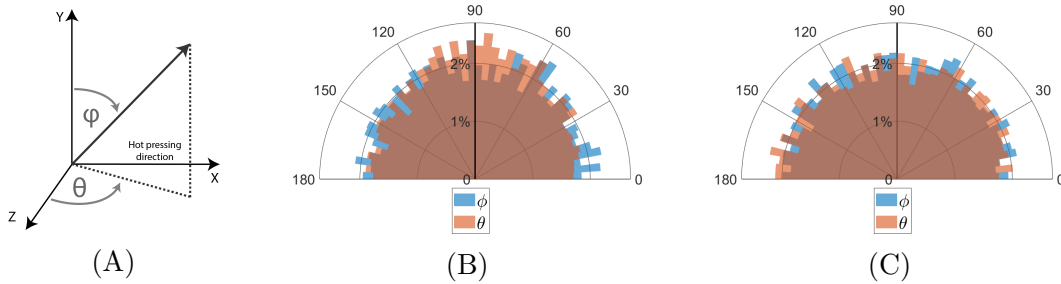


Figure 2.5: A) Spherical coordinate convention for orientation. B) AD85 nearest neighbor orientation polar histogram. C) AD85 pore major axis orientation polar histogram. The blue and orange represent the ϕ and θ distributions, respectively. The black line at 90° represents the long dimension of the sample.

Figure 2.5C shows the normalized polar histogram for the major axis orientation for sample AD85 01. In both the ϕ and θ distributions, all angular bins have frequencies between 1.7% and 2.5%, with no clear preference for any set of angles. Based on these distributions, the major axes of pores in AD85 are determined to be oriented randomly. The processing that causes slight anisotropy in the spatial distribution of pores does not appear to cause observable anisotropy in the orientation of individual pores.

2.3.4 Spatial Distribution of Pores

To assess the spatial distribution of pores, we first examine the nearest neighbor distribution. The nearest neighbor distance was found to be well

represented by a normal distribution with a mean spacing of $23.1\ \mu\text{m}$ and a standard deviation of $4.2\ \mu\text{m}$. The low standard deviation shows that the nearest neighbor spacing is tightly controlled. Comparisons of the observed distribution against the spacing in the Poisson point distribution provided an average of $Q = 1.21 \pm 0.06$ and $R = 0.37 \pm 0.03$, respectively. This indicates that the mean spacing is greater than that of a random distribution while the observed variance in spacing is much lower than that of a random distribution. Taken together, these parameters indicate that the defects are generally regularly distributed.

Beyond global patterns, Voronoi tessellation was applied to investigate local spatial characteristics in the microstructure. Figure 2.6 shows a scatter log-log plot of Voronoi cell volume as a function of pore size. The contour indicates normalized frequency, with cooler colors indicating lower frequency and warmer colors indicating higher frequency. The cell volume, which can be thought of as the region of influence around a pore, is plotted against pore size to investigate the relationship between size and spacing. Between cell volumes of $1.8 \times 10^4\ \mu\text{m}^3$ and $1 \times 10^5\ \mu\text{m}^3$, there is a tight concentration of data points in Figure 2.6 for all pore sizes. The horizontal band in Figure 2.6, outlined by the dashed lines, indicates that the average spacing between defects is largely independent of size, and the consistent cell volume is in agreement with the regular distribution predicted by the nearest neighbor method. The scatter about the band is the greatest near a pore size of $14\ \mu\text{m}$ and decreases gradually as pore size increases. This shows that the spacing around pores becomes more regular as the pore size increases. Of the pores that deviate from the band, most exhibit larger cell volumes than those in the band. Since larger cell volumes represent pores that are farther from near neighbors, this suggests that the sparser regions are typically occupied by smaller defects, while the majority of defects exist in higher density regions.

2.3.5 Mechanical Testing

A key advantage of DIC strain measurements is the access to spatial distribution of strains, which allows for evaluation of stress equilibrium and con-

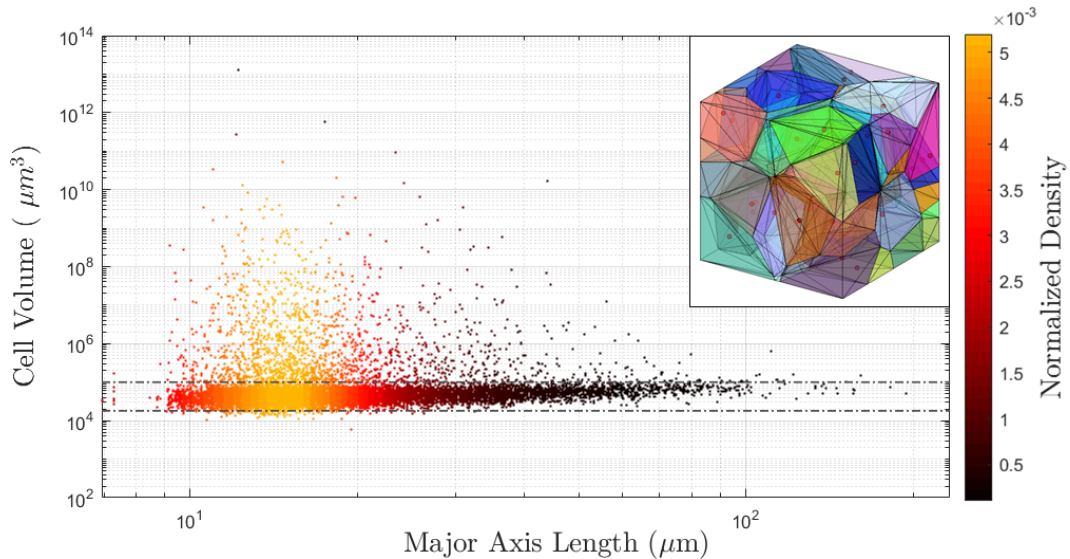


Figure 2.6: Log-log plot of Voronoi cell volume as a function of pore major axis length in AD85. Contour shows normalized density. Dashed lines indicate boundaries to the high frequency band where the majority of data points lie. The inset is a visualization of Voronoi tessellation where the red dots are seed points.

firmation of a good Kolsky bar experiment. Others have checked for stress equilibrium by comparing the front face stress, computed using the incident and reflected waves, to the rear face stress, computed using the transmitted wave[67]. To illustrate the process of checking for stress equilibrium in our experiments, Figure 2.7 shows the stress and strain histories for a dynamic compression test matched up in time. A range of strain profiles are shown, each representing a different area of interest (AOI) on the surface of the sample as indicated by the inset in Figure 2.7. The average strain history was computed by averaging the strain over the entire surface, and this strain is used later in stress-strain plots in Figure 2.8. The stress, computed from the transmitted bar signal, is a measure of the bulk response of the specimen, while the strains are computed from only one surface, with more local measurements being accessible through DIC. Therefore, while agreement between strain profiles from different regions is representative of good equilibrium on the sample surface, agreement between the normalized stress and strain curves in Figure 2.7 serves as a further indicator of stress equilibrium in the sample.

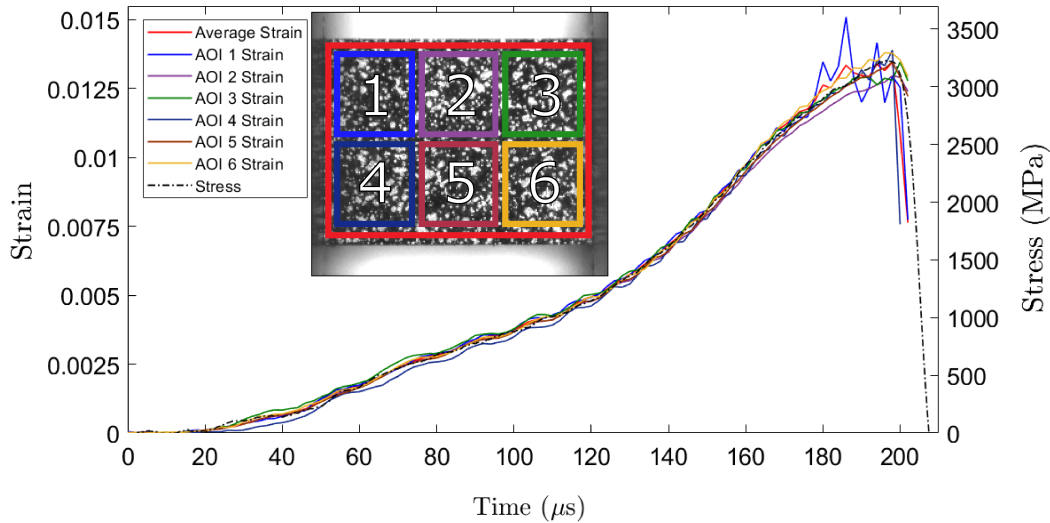


Figure 2.7: Strain profiles from DIC are matched up to the stress profile computed from the transmitted gauge. The inset shows the area of interest (AOI) each strain profile is computed from. The red strain profile is the average of the entire face.

Greater agreement was found between the different AOI's for the dynamic tests than for the quasi-static tests in this study. One advantage of using smaller specimens is that the surface to volume ratio increases, so the surfaces that are imaged during the compression experiments are more representative of the bulk behaviour. In most dynamic tests, chipping was observed at the edges and corners of the sample as the strain accumulated, but typically the sample surface remained plane and nominally intact by the time peak strain is reached. For the test shown in Figure 2.7, chipping occurs at the top left corner of the sample, leading to a destabilization of the strain field in AOI 1 at 180 to 200 μs . This is responsible for the fluctuations in the AOI 1 strain profile near the peak strain, and, in general, strain profiles deviate the most near the peak strain. Following peak strain, the sample surface remains plane and intact for up to 4 frames before significant cracking and fragmentation occurs. These framing rates therefore allow for some strain measurements of the post-peak relaxation of the material.

The combined quasi-static and dynamic stress-strain curves across all experiments are shown in Figure 2.8. The strain rates in all experiments were computed using a linear fit of the strain-time profile obtained through DIC.

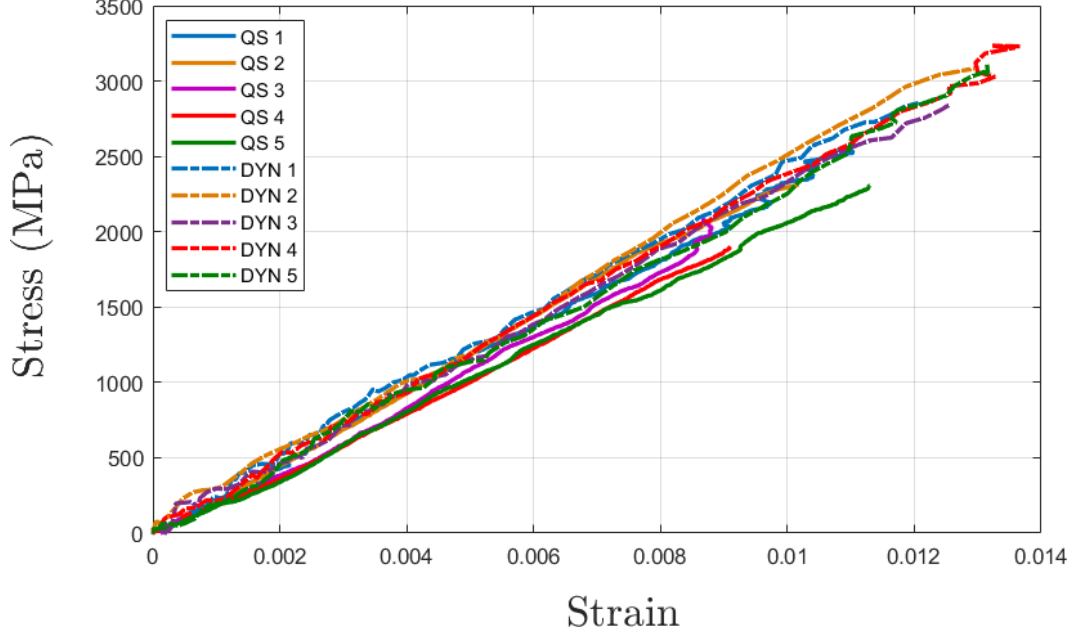


Figure 2.8: Stress-strain curves for the quasi-static (solid line) and dynamic (dashed line) compression experiments of AD85 alumina.

The strain rates ranged from 2.0 to $2.2 \times 10^{-4} \text{ s}^{-1}$ in the quasi-static experiments and 6.8 to $8.9 \times 10^1 \text{ s}^{-1}$ in the dynamic experiments. The stiffness was obtained by taking the slope of the stress-strain curves. Table 2.2 shows the peak compressive strength, stiffness, and failure strain for all experiments. In this study, the quasi-static strength was found to be $2.24 \pm 0.23 \text{ GPa}$. Arrowood and Lankford[16] have reported a similar compressive strength of 2.14 GPa for cylindrical AD85 specimens of a comparable size (6.36 mm diameter by 13.36 mm in length) tested at a strain rate of $1.1 \times 10^{-4} \text{ s}^{-1}$. With the increase in strain rate in the dynamic tests, the compressive strength increases to $3.04 \pm 0.16 \text{ GPa}$, and the failure strain also increases from $1.01 \pm 0.10\%$ at quasi-static to $1.29 \pm 0.05\%$ in the dynamic tests. This rate-dependent behaviour is well documented in ceramics[68, 69]. The stiffness was measured to be $224 \pm 12 \text{ GPa}$ in the quasi-static tests and $235 \pm 6 \text{ GPa}$ in the dynamic tests. Though the loading technique is slightly different between the two rates, the stiffness is consistent within scatter. Both the strength and stiffness are comparable to the manufacturer values in Table 2.1.

To quantify the variation across the two strain rates, we examine the coef-

efficient of variation (COV), a relative measure of variation which is defined as the ratio of the standard deviation to the mean. Summarized in Table 2.2, the COV for stiffness, strength, and failure strain are 5.30%, 10.28%, and 10.30% in the quasi-static tests. The corresponding COV values are 2.54%, 5.20%, and 4.17% in the dynamic tests. The low COV values show relatively low variability in the mechanical properties. In general, it was found that greater peak stress corresponded to greater stress equilibrium in the specimen, which points to one source of variability in the mechanical results. Comparing the variability in properties between two strain rates, it can be seen that the COV values in the dynamic tests are roughly 50% lower than those in the quasi-static regime. The implications of these results are discussed next.

Table 2.2: Summary of stiffness, strength, and failure strain in quasi-static (QS) and dynamic (DYN) compression experiments with coefficient of variation (COV).

Sample	Stiffness (GPa)	Strength (GPa)	Failure Strain
QS 1	230	2.583	1.10%
QS 2	241	2.311	1.02%
QS 3	227	2.087	0.87%
QS 4	212	1.901	0.91%
QS 5	209	2.306	1.13%
QS Average	224	2.238	1.01%
QS Standard Deviation	12	0.230	0.10%
QS COV	5.30%	10.28%	10.23%
DYN 1	239	2.855	1.21%
DYN 2	241	3.146	1.29%
DYN 3	234	2.844	1.26%
DYN 4	237	3.230	1.37%
DYN 5	224	3.109	1.31%
DYN Average	235	3.037	1.29%
DYN Standard Deviation	6	0.158	0.05%
DYN COV	2.54%	5.20%	4.17%

2.4 Discussion

This paper presents microstructural and mechanical characterization results on AD85 alumina, focusing on variability in the internal pore distribution and mechanical properties. Meso-scale internal pores were visualized

using XCT, and a number of methods for interpreting 3D digital reconstructions have been applied to characterize the pore distribution. The mechanical response of the scanned material has been probed at quasi-static and dynamic rates. In the discussion section, we explore the microstructural characterization methods and their applications in the context of manufacturing and computational model parameters, then we assess the variability observed in the AD85 microstructure and uniaxial compression results.

2.4.1 Manufacturing

This study contributes to a growing body of work focused on the utilization of XCT as a 3D quantitative characterization tool[27, 29]. While spatial and contrast resolution in XCT have advanced to allow for the *visualization* of microstructural features, *characterization* requires methods for interpreting the reconstructed 3D data. The methodology presented in this paper can be applied to characterize pores or secondary phase particles in a range of materials, including composites, advanced ceramics, foams, and certain metal alloys. In all of these materials, it is important to control the spatial heterogeneity in the microstructure for the development of enhanced mechanical properties. The XCT spatial characterization methods presented serve as powerful indicators of spatial heterogeneity, allowing for the characterization of the type of spatial distribution as well as the extent of variability in spacing. Using these methods, manufacturing parameters or processes can be linked to the spatial characteristics of the resulting microstructure. Since XCT is non-destructive, manufacturing parameters and spatial distributions can further be linked to mechanical properties of the characterized material, ultimately enhancing our understanding of the relationships between processing, structure, and property.

As an example, consider the regularity in pore spacing found in AD85. X-ray diffraction analysis of AD85 performed by the authors in Sano et al.[34] has identified Mg_2SiO_4 as a secondary phase in the microstructure, which indicates that magnesia and silica were introduced as additives during sintering. Gavrilov et al.[70] investigated the microstructure of alumina co-doped by mag-

nesia and silica and linked Si/Mg ratios less than unity to greater uniformity in the microstructure. These findings, based on qualitative analysis of SEM images of the microstructure in the Gavrilov study[70], are consistent with the spatial homogeneity characterized in the alumina in the present study. Using the R and Q parameters from nearest neighbor comparisons and Voronoi tessellation, not only can we confirm uniformity in the microstructure, but we can also quantify the *degree* of uniformity relating to, for example, different ratios of Si/Mg. This example shows how the XCT characterization methods presented can be utilized in the optimization of processing parameters for the manufacturing of materials.

2.4.2 Parameters for Computational Models

Recent studies are making efforts towards introducing distributions of defect characteristics where computational models describing the properties or failure of porous materials have traditionally employed single parameter defect characteristics such as average defect size or defect density. Paliwal and Ramesh[8] incorporated flaw size and orientation distributions in their model for interacting flaws. Graham-Brady[32] investigated the use of Monte-Carlo simulations as a method for introducing spatial variability into failure models. Levy and Molinari[23] implicitly modeled variability in microstructure by assigning fracture activation thresholds from different probability distributions to the defect population. However, despite theoretical efforts to incorporate variability and distributions of microstructural characteristics, experimental observations of these characteristics are limited in the literature, and simulations in the above studies are commonly performed using assumed or idealized distributions. The characterization methods and results presented in this study are aimed at filling this gap in characterization data, particularly for the characteristics that have received little attention, such as defect spacing and morphology. Where density is a limited representation of defect spacing, the Voronoi tessellation method presented provides direct measurements of distributions of average spacing around individual pores. Ellipsoid representation allows for the quantification of pore morphology as well as orientation

(via major axis orientation) and size distributions. Since all of these characterization tools can be applied simultaneously to the reconstructed defects, multiple characteristics can be assigned to an individual pore (i.e., it is possible to know the size, shape, orientation, and average spacing around a given pore). Therefore, defect characteristics no longer form disjointed descriptions of a single defect population. Instead, the various characteristic distributions that describe a defect population can be incorporated wholesale, and links between characteristics can be analyzed. As an example, the Voronoi tessellation results for AD85 (Figure 2.6) has shown that larger pores typically occur in denser regions while smaller defects experience greater variability in spacing. When incorporated into a model, these relationships provide a higher fidelity representation of the true microstructure than general characteristics.

2.4.3 Variability in Microstructure and Properties

XCT analysis in this study has shown that modern advanced ceramics can be produced with very consistent microstructures. The microstructure of the material under investigation has shown low variability across a range of characterization parameters based on pore size, spatial distribution, orientation, and morphology. The pore size distributions shown in Figure 2.3 are nearly identical across all specimens, with median pore size values ranging from $16.0\ \mu\text{m}$ to $17.2\ \mu\text{m}$ across ten samples, and so the defect size is well-controlled. In terms of spacing, the coefficient of variation for the mean nearest neighbor distance, computed using ten specimens, was found to be 5.7%, indicating low variation in interpore spacing. Nearest neighbor classification based on the R and Q parameters also consistently indicated regular spacing across all samples. Other qualitative characteristics such as the preferred orientation in nearest neighbors and the prolate spheroidal morphology of pores have been repeatably observed in multiple samples. The low variability observed in the microstructure suggests that the mechanical properties should also exhibit low variability. In particular, given the regularity in pore spacing, and therefore the absence of pore clustering, the scatter in strength is expected to be low. The low coefficients of variation for strength, failure strain, and stiffness in

this study confirm that there is a low level of mechanical variability across the 10 specimens, although there is a difference in variability at the quasi-static and dynamic strain rates.

The discrepancy in the mechanical variability between the two strain rates may in part be attributed to variability in testing conditions (e.g. misalignment of platens). Adams and Sine[71] have emphasized that for advanced ceramics, where the tensile strength is much lower than the compressive strength, minor deviations from parallel loading can introduce tensile stresses that cause the specimen to fail well before the compressive strength is reached. More recently, Swab et al.[72] showed that significantly higher quasi-static strength values than are typically reported for boron carbide can be obtained through the use of dumbbell shaped specimens in well-controlled experiments. While all the tests were conducted using identically processed specimens, the parallelism or coaxial alignment of the platens in the MTS load frame used in the quasi-static experiments are different than those of the incident and transmitted bars in the dynamic experiments. Analysis of the strain fields obtained through DIC revealed that the level of stress equilibrium in the sample varies from test to test, and in general, specimens that reached greater peak stress tended to exhibit a higher level of agreement between strain profiles obtained from different regions. This may partially explain the lower variability observed in the dynamic tests, as the stress equilibrium in the dynamic experiments was found to be qualitatively superior than in the quasi-static experiments.

At the same time, the mechanism that is responsible for the rate-dependence of strength in ceramics may also contribute to the difference in variability between the two strain rates. For brittle materials under compression at quasi-static rates, it is often noted that failure is caused by the activation and growth of micro-cracks from the "weakest link" defect[73, 74]. Typically, the critical defect is assumed to be the largest defect in the specimen because the stress required to initiate a micro-crack decreases with increasing defect size. During dynamic compression, the high loading rate may exceed the growth rate of the micro-crack from the critical defect, and as a result, a greater proportion of the defect population may be activated[3, 75]. The growth and interaction of

the total set of micro-cracks eventually lead to macroscopic failure of the specimen[8, 76]. Therefore, while quasi-static failure is thought to be controlled by the size of the critical defect, dynamic failure may have a greater dependence on the overall defect distribution. Based on the XCT measurements of pore size in the present study, even though the size distributions are similar across all samples, the extreme ends of the size distribution can vary significantly. The maximum pore size in the 10 specimens were found to range from 148 to 367 μm , so the largest pore quantified in one specimen may be over 50% larger than the largest pore in another specimen. Consequently, the larger scatter in the quasi-static properties may in part be explained by the greater variation in the maximum defect size in the samples, while the lower variability in the dynamic properties may be attributed to the consistent pore size distribution for sizes less than 36.5 μm across all samples.

2.5 Conclusion

Defect characterization is central to the development of improved advanced ceramics. In the present study, XCT and DIC were used to explore the microstructure and mechanical response of AD85 alumina. The microstructure was found to be consistent across multiple characterization parameters based on pore size, spatial distribution, orientation, and morphology. Spatial analysis methods based on nearest neighbors and Voronoi tessellation were applied to characterize the inter-pore spacing as highly regular and size independent. The characterization methods and results presented can be applied in the design of tailored ceramic microstructures and as improved computational model inputs. Uniaxial compression tests were performed to characterize the mechanical response of AD85, and the variability in the mechanical properties was found to be greater at quasi-static rates than at dynamic rates. The lower variability in the dynamic mechanical properties is attributed to the greater equilibrium achieved in the Kolsky bar tests as well as to the activation of a greater number of pores during loading.

2.6 Acknowledgment

This research was sponsored by the Army Research Laboratory and was accomplished under Cooperative Agreement Number W91NF-16-2-0079 and W911NF-17-2-0213. The views and conclusions contained in this document are those of the authors and should not be interpreted as representing the official policies, either expressed or implied, of the Army Research Laboratory or the U.S. Government. The U.S. Government is authorized to reproduce and distribute reprints for Government purposes notwithstanding any copyright notation herein. The authors would also like to express their thanks to Bernie Faulkner, Rick Bubenko, Haoyang Li, and Kapil Bhagavathula for their help in conducting the experiments.

Research described in this paper was performed at the BMIT facility at the Canadian Light Source, which is supported by the Canada Foundation for Innovation, Natural Sciences and Engineering Research Council of Canada, the University of Saskatchewan, the Government of Saskatchewan, Western Economic Diversification Canada, the National Research Council Canada, and the Canadian Institutes of Health Research. We acknowledge Sergei Gasilov and Ning Zhu for their help in obtaining and reconstructing the XCT scans.

Chapter 3

Deformation Mechanisms and Evolution of Mechanical Properties in Damaged Advanced Ceramics

Calvin Lo^a, Tomoko Sano^b, James D. Hogan^a

^a*Department of Mechanical Engineering, University of Alberta, AB T6G 2R3, Canada*

^b*Weapons and materials Research Directorate, Army Research Laboratory, Aberdeen Proving Ground, MD 21005, USA*

Abstract

We investigated the uniaxial compressive behavior of damaged and intact alumina using quantitative X-ray computed tomography (XCT) analysis coupled with digital image correlation (DIC) for mechanical characterization. Internal three-dimensional crack characteristics such as crack surface area and orientation were quantified using XCT to assess the level of damage. From the quasi-static and dynamic stress-strain results, the primary effects of crack damage is to reduce the initial stiffness and the rate of lateral expansion in damaged alumina. With increasing axial strain, crack closure was found to lead to a recovery of elastic properties, in some cases to intact levels, in the damaged specimens. Near the failure strain, the mechanical response is characterized by a higher rate of lateral expansion and a loss of stiffness due to new crack growth. Localized deformation mechanisms related

to the crack structure, including lateral crack closure, axial crack opening and closing, and inclined crack sliding, were visualized in-situ, and the localized strains on the imaged surface from DIC were found to coincide directly with the reconstructed crack network from XCT. Dynamic compressive strength was found to decrease with increasing crack surface area while quasi-static strength was found to be comparable for damaged and intact specimens. High-speed imaging also revealed differences in fracture behavior between damaged and intact alumina under dynamic compression, with damaged specimens exhibiting a mixed fracture mode that included axial splitting and failure along pre-existing cracks.

Keywords: X-ray computed tomography microstructure digital image correlation damage ceramic crack

3.1 Introduction

Advanced ceramics are commonly used to protect against ballistic threats due to their high hardness and compressive strength. In these applications, ceramic armor may be expected to defeat multiple ballistic projectiles[77], commonly referred to as “multi-hit” capability. During an impact event with a high speed projectile, the ceramic material immediately in front of the projectile often becomes comminuted, and extensive cracks develop and propagate across the surrounding region[2]. In-situ visualization of edge-on impact experiments have shown that the rate of damage propagation in brittle materials, such as glass or ceramics, far exceeds the penetration velocity of projectiles[78]. Other studies focusing on the propagation characteristics of failure fronts in brittle materials include work by Bourne et al.[79, 80] and Partom[81]. Flash x-ray photography of long rod penetration experiments with glass have also shown that penetration is outpaced by the failure front, and the projectile penetrates into damaged material[82]. Johnson and Holmquist[83] have emphasized the important role of parameters relating to damaged and failed materials for accurate impact modeling. As a result, an understanding of the behavior of damaged advanced ceramics, as well as the transition from intact to damaged material behavior, is critical to the development of improved impact models and protection products with increased multi-hit resistance. This is explored in this paper.

The lack of model parameters for damage models has motivated numerous studies focused on the behavior of damaged brittle materials[84–86]. A common approach in the literature has been to pre-damage the ceramic, followed by compression testing on the pre-damaged specimens[87, 88]. Following this approach, quasi-static confined compression experiments have been performed on a range of damaged brittle materials, including SiC-N[89], boron carbide[88], borosilicate glass[87, 90–92], and soda lime glass[93]. Typically, damage in these studies was introduced through thermal shock cycles[88], mechanical load-unload cycles[90], or a combination of both[90]. In their study, Zurek and Hunter[94] performed high strain rate confined compression exper-

iments on pre-damaged TiB_2 specimens using a split-Hopkinson pressure bar (SHPB). The TiB_2 specimens were pre-damaged through a flyer plate impact experiment in order to simulate the damage achieved through shock compression. In an alternative approach, Chen and Luo[95] employed two consecutive compressive waves in a modified SHPB setup to characterize the dynamic behavior of damaged alumina[96] and silicon carbide[97] under confinement. In this technique, the first wave is used to pre-damage the ceramic in-situ under dynamic compression, and the second wave is used to probe the strength of the damaged ceramic. Effort was made to vary the level of damage in all of the above studies (e.g. modifying the number of thermal shock cycles, mechanical loading cycles, shock pressure, or compressive pulse amplitude) to access different damage levels, and microscopy was often used to confirm the presence of cracks where possible. However, limited information exists on quantitative measurements of internal damage[98] and on the uniaxial compressive behavior of damaged ceramics, a configuration which is more favorable for in-situ visualization as compared to triaxial confined compression where the specimen surface is covered.

In this paper, we combine microstructural characterization and in-situ visualization to explore the compressive behavior of pre-damaged advanced ceramics. We apply X-ray computed tomography (XCT) to characterize the internal crack networks of pre-damaged alumina in order to quantify the damage level prior to testing, including crack surface area and orientation. Following damage characterization, quasi-static and dynamic compression experiments were performed to probe the mechanical response of pre-damaged specimens. The dynamic experiments were visualized in-situ using an ultra-high-speed camera to observe the failure process, and digital image correlation was employed to perform spatial strain measurements that allowed for the observation of localized deformation features in the experiments. Finally, the crack characteristics are coupled with the experimental results to connect local deformation mechanisms to the evolution of mechanical properties in damaged ceramics. This work builds on prior work by the authors where a similar approach has been applied to pre-damaged boron carbide[99] and intact alumina[11].

3.2 Experimental Method

3.2.1 Material and Specimen Preparation

The characterization and experiments in this study were carried out on AD995 alumina from Coorstek Inc. (Vista, California, US), with a manufacturer specified density of 3.90 g/cm^3 , Young's Modulus of 370 GPa, and a Poisson's ratio of 0.22. Alumina (Al_2O_3) was chosen as a model advanced ceramic as it is commonly utilized in body armor applications, and has been well studied in the literature [100–102]. The “995” refers to a nominal composition of 99.5% Al_2O_3 , with the other 0.5% being comprised of silicon dioxide[34].

Cuboidal specimens measuring 2.3 mm by 2.7 mm by 3.5 mm were machined from as-received AD995 tiles. The dimensions of the specimens were selected to accommodate both the size of the SHPB used for dynamic compression and the scan volume of the synchrotron X-ray source used for computed tomography scans. The cuboidal shape was chosen so that a flat surface can be visualized during the compression experiments for digital image correlation analysis and tracking of deformation evolution during testing, as will be discussed later in the Mechanical Testing section.

To introduce pre-damage to the specimens prior to the compression experiments, each specimen was subjected to thermal shock cycles. Using a butane blow torch, each specimen was heated to above $750\text{ }^\circ\text{C}$ and then quenched in room temperature water. The number of thermal cycles, ranging from 1 to 8, was varied from specimen to specimen in order to introduce a range of damage levels amongst the different specimens. Cracks caused by the thermal cycles can be observed in the XCT scan of a pre-damaged specimen in Figure 3.1A, as discussed in more detail in later sections. While the thermal cycles were sufficient to cause internal cracking, all pre-damaged specimens remained structurally intact after thermal cycling.

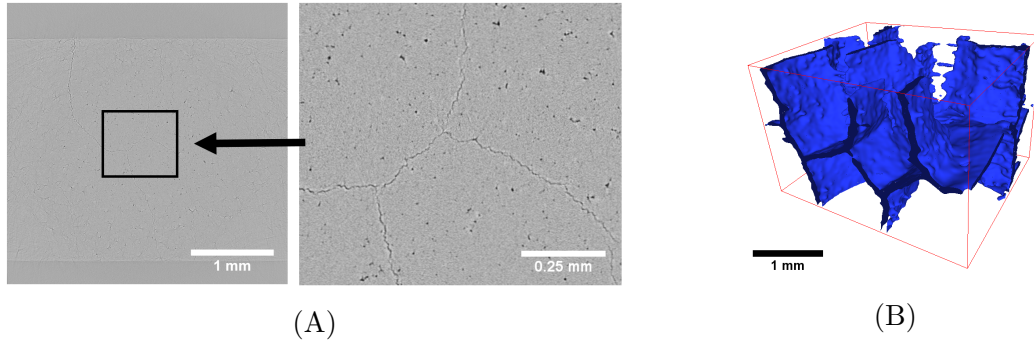


Figure 3.1: (A) XCT scan of AD995 alumina. Due to the high resolution of the scan, small features are difficult to observe under low magnification. A magnified view of the center of the specimen is included on the right to show the internal crack. (B) 3D reconstruction of internal crack network showing the extent and inter-connectedness of the crack network. The red box outlines the boundary of the scan volume.

3.2.2 X-ray Computed Tomography

3.2.2.1 X-ray Computed Tomography Scans

X-ray computed tomography was used to characterize the internal cracks in the pre-damaged specimens. Currently, XCT is capable of visualizing features at sub-micron scales[103], however, there is a trade off between resolution and scan volume; with increasing resolution, scan volume decreases. For this study, it is important to have the resolution high enough to resolve internal cracks, which have crack widths on the order of several microns, but also a scan volume large enough to encompass the test specimen and avoid sampling issues. A partial scan may not accurately capture a representative level of damage since the cracks are not necessarily uniformly distributed throughout the volume of the samples. Based on these considerations, the specimens were scanned with a resolution of $1.75\ \mu\text{m}$ and a scan volume spanning $2.196\ \text{mm}$ by $3.413\ \text{mm}$ by $3.413\ \text{mm}$, which is approximately 93% of the total specimen volume. All XCT scans were performed using the Skyscan micro-CT system on the 05ID-2 POE-2 endstation[104] at the Biomedical Imaging and Therapy (BMIT) beamline at the Canadian Light Source synchrotron facility (Saskatoon, Saskatchewan, Canada). Ring artifacts were removed using a low-pass Gaussian filter[105]. Figure 3.1A shows a reconstructed XCT scan for a

pre-damaged AD995 specimen. Macroscopic cracks can clearly be seen in the magnified view, and SEM has confirmed that the small dark features in the XCT scans are internal pores[11].

3.2.2.2 Image Segmentation and Post-processing

To reconstruct the crack networks digitally, the first step is to apply image segmentation to isolate the cracks in the XCT scans. During image segmentation, the pixels that represent the features of interest, in this case, cracks, are segregated to form binary images where foreground pixels (1's) represent crack area and background pixels (0's) represent other constituents. Note that the small unconnected pores are not to be included in the reconstruction because they are present in the intact material. Cracks are the only form of structural damage considered in this study. An entropy filter[106] is applied to the grayscale image to enhance the crack edges in the scans, and then locally adaptive thresholding[36], computed using the mean intensity of the grayscale values in the neighborhood of each pixel, is applied to segment the grayscale image.

Following segmentation, a number of 2D filtering and processing operations are required to remove noise and other microstructural constituents from the binary image. Non-physical features may be introduced to the binary image due to over-segmentation or scan artifacts, and these are typically in the form of salt and pepper noise[107]. Owing to the grayscale difference between the pores and the surrounding alumina grains, the pores also become segmented into the foreground. In addition, due to local variations in the scan contrast, the crack area may not be fully segmented, leading to gaps in the binarized crack network. To distinguish crack area from pores and point-like over-segmentation noise, all of the objects in a binary image are filtered based on a combination of object area, aspect ratio, and extent. *Extent* is the ratio between the object area and the area of the bounding box. For the pores and point-like noise, the area is small, and both the extent and the aspect ratio are expected to be close to unity. In contrast, long connected cracks are expected to have a larger area, a lower aspect ratio, and a lower extent. These filters

are applied in combination using logical ‘AND’ to prevent the exclusion of unconnected crack areas which may be small but have a low aspect ratio.

After post-processing, the binary images are combined into a 3D binary matrix, and connected components analysis is performed (using 26 connectivity) to identify the 3D objects formed by the 2D binary slices. From the XCT scan in Figure 3.1A, it can be seen that the cracks are on the scale of the specimen and are much larger in volume than individual pores. Therefore, the reconstructed 3D volumes were filtered based on volume to further remove any pores or noise that were not removed during 2D filtering. As mentioned previously, the crack area in each XCT scan may not be fully segmented, and this can lead to gaps in the 3D reconstructed crack network. To fill out the gaps and complete the crack network, morphological closing was applied to the 3D binary matrix. Morphological closing[108] involves the dilation of a binary matrix by a structuring element followed by the erosion of the dilated matrix by the same structuring element. It is attractive in this application because it systematically dilates the binary object, closing any gaps, and then erodes the dilated object to return the object to its original size with the gaps closed. A spherical structuring element was used to preserve the shape of the crack network. A render of the final reconstructed crack network for one specimen can be seen in Figure 3.1B. The red box indicates the boundary of the XCT scan volume. It can be seen that the cracks are largely planar, span much of the sample, and are well connected. For each specimen, connected components analysis revealed that the reconstructed objects are few in number but large in volume, which confirms that the cracks are mostly connected.

3.2.2.3 Crack Characterization

Due to the complexity, interconnectedness, and randomness of the crack networks in the pre-damaged specimens, the effects of crack damage may be assumed to be isotropic, in which case a scalar damage metric would be appropriate. Scalar metrics for characterizing cracks include crack density, volume, and surface area. Landis[98] and Oesch et al.[109] have investigated crack surface area and volume as scalar damage metrics in in-situ XCT investiga-

tions of concrete. Crack density, typically used to consider micro-cracks[8], is not applicable in this study since the cracks are large and interconnected. With increasing thermal cycles, the cracks become more interconnected and the number of cracks actually decrease. Based on analysis of individual scans, crack widths range from $3\ \mu\text{m}$ at the thinner range to $70\ \mu\text{m}$ for the larger cracks. Given the resolution of the scans, it is difficult to distinguish between a closed crack and a crack width less than $3\ \mu\text{m}$. However, due to the X-ray attenuation at the free surface, these thin cracks can still be distinguished by their grayscale contrast. Therefore, crack volume measurements may be over-estimated by the inclusion of closed or thin cracks. While closed cracks may not contribute to the total crack volume, they are expected to have an effect on the mechanical response. As a result, surface area may serve as a better crack characteristic in this type of specimen configuration in comparison to crack volume because it can be accurately quantified for thin cracks.

Alternatively, anisotropic local deformation related to the internal cracks, such as frictional sliding or crack closure, will depend on crack orientation[39, 110]. Traditional definitions for crack orientations are based on the crack normal, which is easy to compute for idealized planar cracks. However, three-dimensional cracks may branch off, reconnect, and curve, as shown in Figure 3.1B. This complicates the process of determining a crack normal, as the reconstructed cracks in these types of specimens are well connected and seldom planar. The crack network must be discretized for the quantification of crack normals. To do this, we apply the Marching Cubes algorithm[111], a technique for generating an isosurface from a three-dimensional binary matrix that is commonly used to visualize XCT data[112]. Marching Cubes produces a mesh comprised of triangles, from which the crack orientation can be computed. Using the vertices of the triangles, we can calculate both the surface normal vector and surface area of the triangle. Once the surface vectors are known, the orientation of the crack surface with respect to any direction can be computed. The orientation of interest in this study is the angle between the loading axis of the specimen (along the 3.5 mm dimension) and the surface normal vector. Since the area of individual triangles are also known, the area

contribution of surfaces with a given orientation can be quantified. The total crack surface area can then be computed by summing over all triangles. Note that the triangles do not all have the same area. To give an idea of the level of discretization, Marching Cubes generates over 2,000,000 triangles for the mesh of one specimen's crack network.

3.2.3 Mechanical Testing

A Material Testing System (MTS) 810 load frame was used to carry out quasi-static uniaxial compression experiments. Samples were compressed along the longest dimension (3.5 mm) using displacement control at a constant rate of 3.5×10^{-3} mm/s, which corresponds to a nominal strain rate of 1×10^{-3} s⁻¹. Based on digital image correlation measurements (methods presented later), the actual strain rate in the quasi-static experiments is lower by an order of magnitude due to the compliance of the load frame. To maintain a uniform stress distribution and prevent indentation, tungsten carbide platens jacketed in titanium were used at the interface between the compression platens and the ceramic samples. High-pressure grease was used to lubricate the platen-ceramic interface and facilitate free lateral expansion. The specimen surface was visualized at 100 frames per second (FPS) at a resolution of 850 by 850 pixels using a Promon U750 high speed camera. This frame rate is insufficient for capturing the fracture process in the quasi-static experiments. Intact specimens were also tested to serve as a reference to the damaged specimens.

A split-Hopkinson pressure bar (SHPB) was used to perform dynamic uniaxial compression experiments. All bars in the SHPB have a diameter of 12.7 mm and are made of maraging steel with a stiffness of 200 GPa and a density of 8100 kg/m³. The incident and transmission bars measure 1000 mm and 910 mm, respectively. As in the quasi-static tests, titanium jacketed tungsten carbide platens and high pressure grease were used at the platen-ceramic interface. The tungsten carbide platens are impedance-matched to the incident and transmitted bars to reduce wave reflection at the interfaces. The incident pulse was created using a 304 mm striker with a tin pulse shaper measuring 3.175 mm in diameter and 1 mm in thickness. This setup produces a trian-

gular pulse with a rise time of 230 μs . During the compression experiments, a Shimadzu HPV-X2 ultra-high-speed camera was used to visualize the surface of the specimen at 500,000 FPS with an exposure time of 500 ns. A total of 128 frames measuring 400 by 250 pixels was recorded for each experiment. This frame rate is capable of capturing the failure and post-peak fragmentation process.

Digital image correlation (DIC) was used to make strain measurements at both quasi-static and dynamic rates. Two-dimensional DIC is an established method for strain measurement and has been applied to study the mechanical response of a range of materials (e.g., composites[60], aluminum foams[61], and mild steels[9]). DIC is a computer vision method that tracks speckle patterns on surfaces to compute deformation fields[62, 63]. Experimental challenges relating to the application of DIC in this study include the generation of a fine speckle pattern required for small specimens and adequate lighting for filming at high frame rates. To address these challenges, an airbrush with a 0.15 mm diameter nozzle was used to produce a fine speckle pattern (i.e. 5 to 10 pixels per speckle) appropriate for DIC measurements. A high power LED array from REL Inc. was used to illuminate the specimen surface during dynamic experiments, and high gloss metallic paint was used to create the speckle pattern to enhance surface reflectivity. VIC-2D (v6 2018) from Correlated Solutions (Irmo, South Carolina, US) was used to perform the DIC analysis. The specimen surface was discretized into 27 x 27 pixel subsets with a step size of 7 pixels. The zero-normalized sum of squared differences correlation criterion and the optimized 8-tap interpolation scheme[64] were used to carry out correlation analysis. Strains were calculated using the engineering strain tensor.

Stress-strain curves were produced by matching the computed strain profiles to the stress histories. The peak strain and peak stress were matched in time through MATLAB to correlate the rest of the strain and stress profiles. Quasi-static stress data was measured using the load cell in the MTS load frame while dynamic stress information was computed using the transmitted gauge signal in the following equation:

$$\sigma(t) = E \frac{A_0}{A_B} \epsilon_T(t) \quad (3.1)$$

where σ is the stress (Pa) in the specimen, t is time (s), E is the Young's Modulus (Pa) of the transmitted bar, A_0 is the specimen cross-sectional area (m^2), A_B is the transmitted bar area (m^2), and $\epsilon_T(t)$ is the strain from the transmitted gauge. The strain rates in all experiments were computed using a linear fit of the strain-time profile obtained through DIC. The strain rates ranged from 1.6 to $2.3 \times 10^{-4} \text{ s}^{-1}$ in the quasi-static experiments and 6.8 to $13.1 \times 10^1 \text{ s}^{-1}$ in the dynamic experiments. The application of 2D DIC for characterizing stress-strain behavior is typically based on the assumption that the surface measurement is representative of the overall strain profile for the specimen[113]. Given the inhomogeneous nature of cracked specimens, it is not strictly accurate to match the stress profile to the strain profile for damaged specimens, as the stress profile is a measure of the overall response to force while the strain profile is a measure of the deformation on only one surface. The deformation of each specimen surface is expected to differ depending on the pre-existing cracks on that surface, so surface measurements may not be representative of the overall response, unlike in intact specimens. Currently, there are limited methods for characterizing the development of inhomogeneous three-dimensional strains under compressive loading. One method is to combine XCT visualization with in-situ compression testing[114]. However, such setups are not easily accessible, and strains cannot be continuously measured due to the time required to perform XCT scans, during which the specimen may also relax. In addition, XCT scan times preclude visualization of ceramics under dynamic compression. For these reasons, we have chosen to compute the stress-strain behavior of damaged ceramics in this study by matching surface strain measurements to the stress profiles and emphasize that it is an approximation.

3.3 Results

3.3.1 Crack Orientation and Surface Area

First we begin by presenting the crack characterization results. The stacked bar chart in Figure 3.2 shows the crack surface area quantified using XCT for each specimen. Specimens are named with the following conventions: quasi-static tests are denoted by “QS”, dynamic tests are denoted by “DYN”, damaged specimens are denoted by “D” in front of the test number, and intact specimens are denoted by “IN” in front of the test number. The total crack surface area for each specimen is divided into segments showing the area contribution of crack surfaces that form different angles with respect to the loading axis in 10 degree intervals. This is done to illustrate the distribution of crack orientations within each specimen. Overall, the crack area in each orientation interval generally increases as total crack area is increased. As well, there are no major differences between the relative contributions of different crack orientations across most of the specimens. One exception is specimen DYN D1, which has a relatively low amount of crack surface area between 0° and 10° and a relatively large amount of crack surface area between 30° and 40° given its low total crack surface area. The 3D reconstruction for DYN D1 shows that the crack pattern in this specimen is dominated by a large inclined crack, which is responsible for the preference for the angles between 30° and 40° . Cracks with different orientations with respect to the loading axis are expected to have different effects on the deformation of the specimen, as will be shown in Section 3.3.3. With these crack measurements, we can connect the damage in individual specimens to differences in mechanical behavior, such as crack closure transition strains (Section 3.4.1) or compressive strength (Section 3.4.2).

3.3.2 Quasi-static and Dynamic Compression Experiments

Next, we present the quasi-static and dynamic compression results. The stress-strain and lateral-axial strain curves for the quasi-static and dynamic compression experiments are shown in Figure 3.3A and Figure 3.3B, respec-

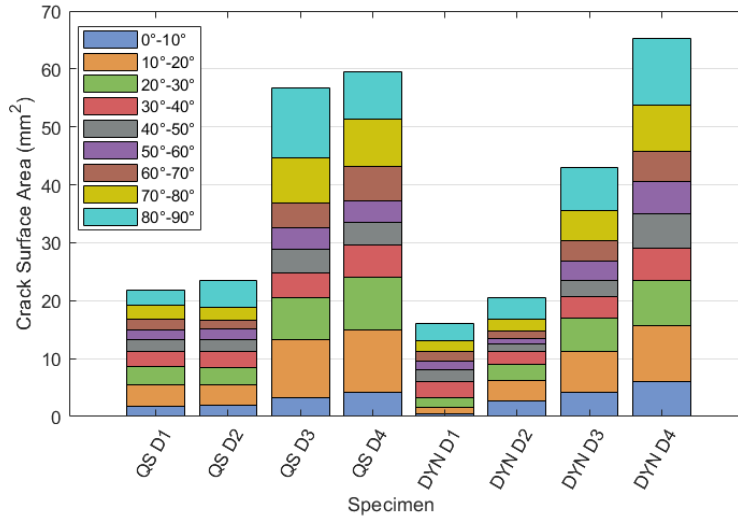


Figure 3.2: Stacked bar graph showing the crack surface area for each damaged specimen (D1 to D4). The quasi-static tests are denoted by QS and the dynamic tests are denoted by DYN. The divisions denote the area contribution of crack faces with different orientations to the loading axis.

tively. The intact specimens exhibit mostly linear elastic behavior at both strain rates, as shown by the linear stress-strain and lateral-axial strain curves. Closer to the failure strain, the intact stress-strain curves deviate from linearity due to surface chipping, which destabilizes the strain field. From the quasi-static experiments, the intact AD995 specimens have an average failure strain of $0.71 \pm 0.05\%$, peak compressive stress of 2.6 ± 0.2 GPa, stiffness of 380 ± 20 GPa, and Poisson's ratio of 0.23 ± 0.02 . From the dynamic experiments, the intact AD995 specimens have an average failure strain of $1.1\% \pm 0.1\%$, peak compressive stress of 3.9 ± 0.1 GPa, stiffness of 370 ± 10 GPa, and Poisson's ratio of 0.24 ± 0.03 . The rate dependent increase in strength and failure strain is well-documented for advanced ceramics[68].

Based on the stress-strain data in Section 3.3.2, it can be seen that crack closure dominates the deformation of damaged specimens at both strain rates during the early stage of compression. Since the pre-existing cracks in the damaged specimens are more compliant than the solid material, the cracks will close over axially before the intact material is compressed. This crack closure behavior is reflected in the stress-strain curves in Figure 3.3A and Fig-

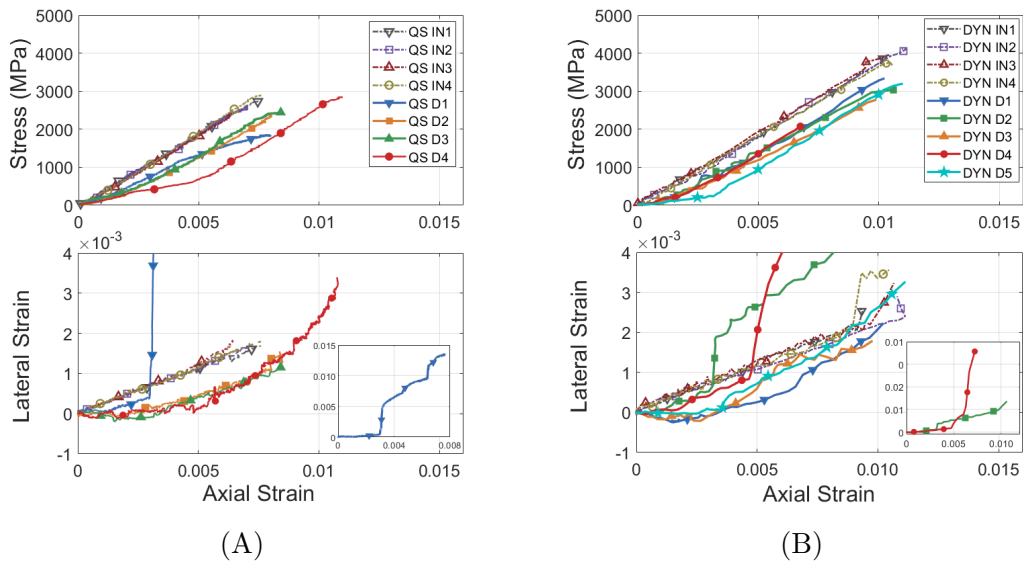


Figure 3.3: Stress-strain and lateral-axial strain curves for intact and damaged specimens tested under (A) quasi-static and (B) dynamic compression. The quasi-static tests are denoted by QS and the dynamic tests are denoted by DYN. Intact tests are represented using dashed lines and denoted by IN while the damaged tests are represented using solid lines and denoted by D. The lateral-axial strain curves for QS D1, DYN D2, and DYN D4 are shown separately in insets so the evolution of the other curves are not dwarfed by the large lateral strains.

ure 3.3B by the low initial stiffness and the subsequent increase in stiffness as the specimens undergo further compression. As the cracks close, the stiffer intact material becomes compressed, thereby increasing the overall stiffness of the specimen. For specimens QS D2, QS D4, DYN D1, and DYN D5 in Figure 3.3A and Figure 3.3B, the increase in stiffness is accompanied by a linearization of the stress-strain curve after closure, and the recovered stiffnesses, ranging from 357 to 387 GPa, are maintained until close to failure. This shows that the intact stiffness may be fully recovered in damaged specimens following crack closure at these damage levels. The lateral strain curves in the lower halves of Figure 3.3A and Figure 3.3B are also consistent with the crack closure interpretation. Since crack volume is expected to dominate much of the initial axial strain, there should be minimal lateral expansion, and this is the case for most of the damaged specimens (e.g., QS D2 and DYN D5). For specimens QS D3, DYN D1, and DYN D3, the initial negative lateral strain suggests that crack closure can actually lead to contraction in some cases, and this is likely due to the orientation of the pre-existing cracks in the specimen (e.g., inclined and axial cracks intersecting at an acute angle). Furthermore, the axial strain at which the lateral strain begins to increase is consistent with the axial strain at which the stiffness markedly increases. After the cracks are closed, the compression of intact material will lead to an increase in overall lateral strain, which should coincide with the increase in stiffness. Though it is more difficult to see in the other specimens, this transition can be clearly observed in Figure 3.3A for specimen QS D4 at an axial strain of 0.48%, and in Figure 3.3B for specimen DYN D5 at an axial strain of 0.40%. For other specimens, such as QS D1 and DYN D2, the intact stiffness is never fully recovered. Instead, the gain in stiffness from crack closure is believed to be offset by the loss of stiffness from the growth of pre-existing cracks or nucleation of new cracks. The large increases in lateral strain shown in the inset on Figure 3.3A are caused by the opening of axial cracks in specimen QS D1 (as will be shown visually later in Figure 3.4A), and each sudden increase correlates with a change in slope for the stress-strain curve.

After crack closure, it can be seen from Figure 3.3A and Figure 3.3B that

the lateral strains rise faster for the damaged specimens than for the intact specimens, which indicates that the rate of lateral expansion in the damaged specimens has exceeded the Poisson's ratio of the intact material. This shows that lateral crack opening is contributing to lateral expansion in addition to the elastic expansion of solid material in the damaged specimens. As well, the softening of the stress-strain curve near the failure strain is accompanied by a sharp increase in lateral expansion for several specimens (e.g., QS D4, DYN D2, DYN D5), indicating catastrophic crack growth leading to macroscopic failure. While the stages may differ in length for each specimen, all the damaged specimens exhibit crack closure, followed by an increase in stiffness, and then a loss of stiffness leading to failure. To the author's knowledge, this has not been noted before in the literature.

Where results from the two strain rate regimes for the damaged materials differ are in the failure strains and in the rate of lateral expansion following crack closure. Pre-existing cracks may degrade the strength of the specimen and cause failure at a lower axial strain. At the same time, the compliance of the cracked regions reduce the overall stiffness of the specimen and allow for greater axial strains to be achieved. The influence of damage on failure strain is controlled by these competing failure mechanisms. In the quasi-static tests, the additional strain from crack closure contribute significantly to the failure strain, as all of the damaged specimens exhibit greater failure strains than the intact specimens. In contrast, the failure strains for the damaged specimens in the dynamic experiments are comparable to or lower than those of the intact specimens, which suggests that the strength degradation is more critical in dynamic loading. In general, the dynamic damaged specimens also show an increased rate of lateral expansion in comparison to the quasi-static damaged specimens, signaling increased crack opening at higher strain rates and, thus, different damage accumulation behavior. Taken together, these differences show that pre-existing damage has a greater effect on the compressive strength under dynamic strain rates than quasi-static strain rates.

3.3.3 Localized Deformation in Damaged Ceramics

Next we examine the DIC strain contours computed from the quasi-static experiments to explore localized deformation features in damaged advanced ceramics. Crack opening can be visualized in DIC by the development of localized positive lateral strain. Shown in Figure 3.4A is a lateral strain contour plot of specimen QS D1, where the opening of a large axial crack can be observed in the figure. This crack opening corresponds to the first large increase in lateral strain for QS D1 at an axial strain of 0.30% in Figure 3.3A and is the cause of the relatively low strength of QS D1 (1.88 GPA vs 2.60 GPa). The second sudden increase in the lateral strain for QS D1, at an axial strain of 0.34% in the inset in Figure 3.3A, is also connected to the opening of a second axial crack on the surface. Shown in Figure 3.4B is a lateral strain contour plot of specimen QS D3, which also has a large axial crack. However, rather than a region of localized positive lateral strain, this crack is outlined by a region of negative lateral strain, which suggests that the crack is actually accommodating the expansion of the adjacent solid material, and the crack does not open throughout the test. This mechanism may compete with crack growth and solid material compression, both of which lead to increased lateral expansion, to reduce the overall lateral expansion of the specimen (i.e., the axial crack becomes closed).

Figure 3.4C shows the surface of specimen QS D4 visualized through XCT. By overlaying the XCT scan in Figure 3.1A with the DIC contours, localized deformation features can be connected to the physical structure of the crack network. The contrast in this XCT scan has been enhanced through an entropy filter[106] to highlight the cracks. Specimen QS D4 is used as a representative sample because it exhibits the different types of localized strains observed for damaged specimens in this study and demonstrates deformation mechanisms associated with different crack orientations. Shown in Figure 3.4D is an axial strain contour plot of QS D4 with the crack pattern overlay. This direct observation of crack closure shows the localized compressive strains that develop at lateral and low-angled inclined cracks under uniaxial compression. The lat-

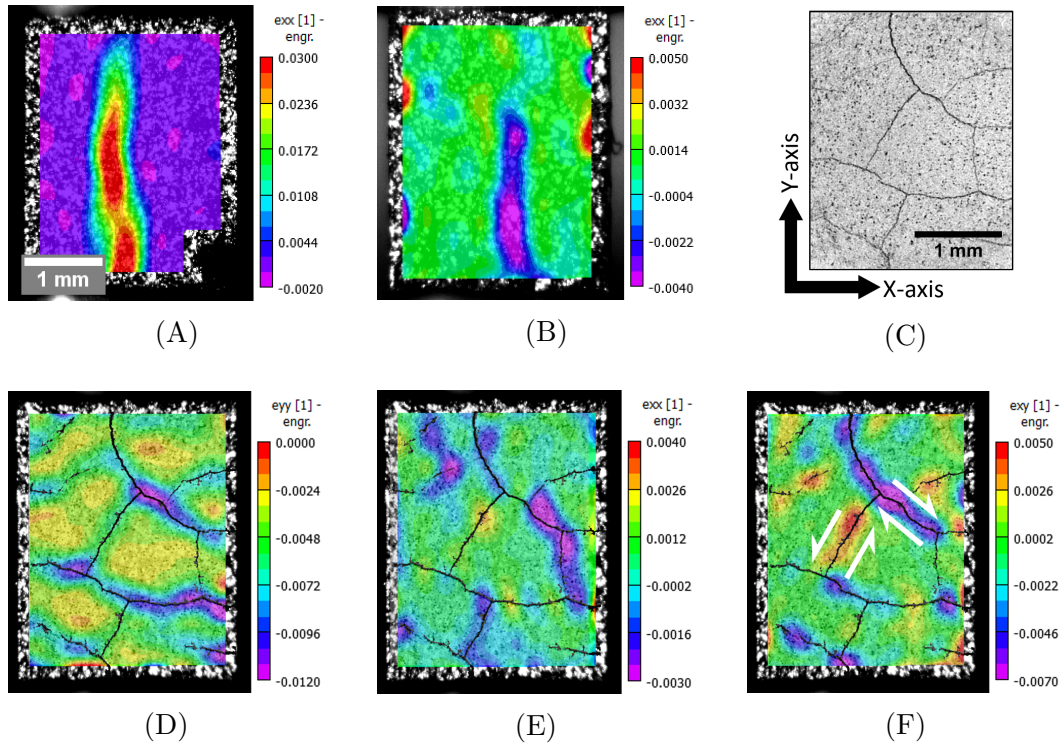


Figure 3.4: (A) Lateral contour plot of QS D1 showing the opening of a large axial crack. (B) Lateral contour plot of QS D3 showing a large axial crack that accommodates the expansion of adjacent solid material. (C) XCT scan of QS D4 cropped and filtered to show the crack network on the surface of the specimen. This image is overlaid with surface contours for QS D4 from (D) to (F) to show the location of localized strains in reference to the crack. (D) Axial contour plot of QS D4 showing localized compressive strains at lateral and low-angled inclined cracks. (E) Lateral contour plot of QS D4 showing the closing of axial and high-angled inclined cracks under compression. (F) Shear contour plot of QS D4 showing shear strains along inclined cracks. The white arrows are included to show relative motion of the crack surfaces.

eral strain contour plot of QS D4 in Figure 3.4E shows negative lateral strains developing at axial and high-angled inclined cracks. Similar to specimen QS D3, the expansion of the nearby intact material effectively closes the axial and high-angled cracks. Under compressive loading, inclined crack surfaces may slide against each other following crack closure, as noted in micro-cracks based micro-mechanical models[39, 115]. This frictional sliding behavior can be observed through the shear contour plot shown in Figure 3.4F. White arrows have been added to Figure 3.4F to show the relative motion of the crack surfaces. Negative shear develops along crack surfaces inclined towards the right edge of the specimen, and positive shear develops along crack surfaces inclined towards the left. These are all examples of how cracks with different orientations can cause localized strains to develop and influence the macroscopic mechanical response of the specimen.

Beyond the spatial variation in strains, DIC was also used to track the evolution of local deformation through time to explore the effects of crack orientation on localized axial and shear strain. Figure 3.5A shows the XCT scan of specimen QS D4 overlaid with 7 regions where the local strains were queried. The 7 regions correspond to a range of different structural features, including solid material, axial cracks, inclined cracks, triple junctions, and lateral cracks. Figure 3.5B shows the temporal evolution of axial strain at each of these locations. First, we note that the triple junction (region 6), which has a relatively large crack volume, and the lateral crack (region 7), which is perpendicularly oriented to the loading direction, deform at the greatest rates. As the angle of the crack with respect to the loading direction is reduced, the rate of axial deformation is decreased, as shown by the two inclined cracks (regions 4 and 5) and the axial crack (region 3). Finally, the intact sections (regions 1 and 2) deform at the slowest rate due to the relatively high stiffness. It is interesting to note that the deformation rates are initially identical for the regions of high compliance; the axial strain profiles for regions 6 and 7 evolve similarly up until a time of 12 seconds, at which point they begin to deviate. Similarly, the separate regions of intact material (regions 1 and 2) experience nearly identical strains throughout the entire experiment.

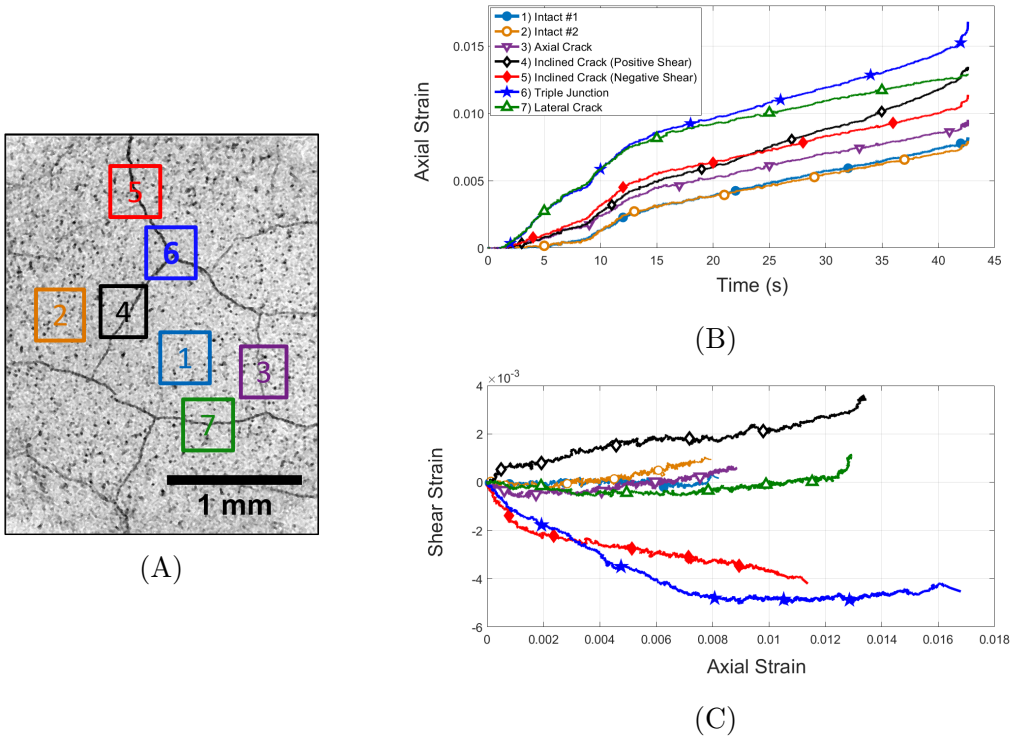


Figure 3.5: (A) XCT scan of QS D4 showing the regions where axial and shear strains are queried. The regions of interest include (1 and 2) intact solid material, (3) an axial crack, (4 and 5) inclined cracks, (6) a triple junction, and (7) a lateral crack. (B) The evolution of axial strain at the regions of interest over time. (C) Shear strain development as a function of axial strain for each region of interest.

To investigate the evolution of frictional sliding between crack faces, shear strain is plotted against axial strain at each of these regions in Figure 3.5C. As expected, there is minimal shear strain at the two intact regions, the lateral crack, and the axial crack. The slopes of the shear-axial strain curves for the triple junction and the inclined cracks indicate that the axial and shear strains are coupled. In other words, crack closure and crack sliding occur simultaneously under loading. Shear strain at the triple junction is arrested at an axial strain of 0.9% and does not develop further under additional axial strain, while shear strain at the inclined crack at region 4 continues to increase until failure. This may explain the divergence in axial deformation between the triple junction and the lateral crack: the shear strain at region 4 continues to accommodate additional axial strain at the triple junction while the lateral strain is constrained by crack closure. Since a frame rate of 100 FPS is insufficient for capturing the fracture process of the specimen, it is not possible to determine which local feature ultimately causes the specimen fail in the quasi-static experiments. As this is only one view of the specimen, it may also be the case that failure is caused by a feature that is not visualized on this surface. In contrast to the quasi-static experiments, where the temporal resolution is limited and the spatial resolution is high, visualization of the dynamic experiments is limited by spatial rather than temporal resolution. While localized strain in the dynamic experiments are also observed in the contour plots generated through DIC, their shapes are not very exact. Therefore, we will not be performing similar analysis with the dynamic experiments.

3.3.4 Failure Process of Damaged Ceramics

With the Shimadzu HPV-X2 imaging at 500,000 FPS, it was possible to capture the post-peak failure process during the dynamic compression experiments. Figure 3.6 shows a comparison of the stress-time histories and failure process for an intact specimen (DYN IN4) and a damaged specimen (DYN D5) under dynamic loading. Red arrows point to the first surface cracks visualized in Figure 3.6. For the intact specimen, the first surface cracks initiate at the right edge of the specimen immediately after peak stress is reached at a time

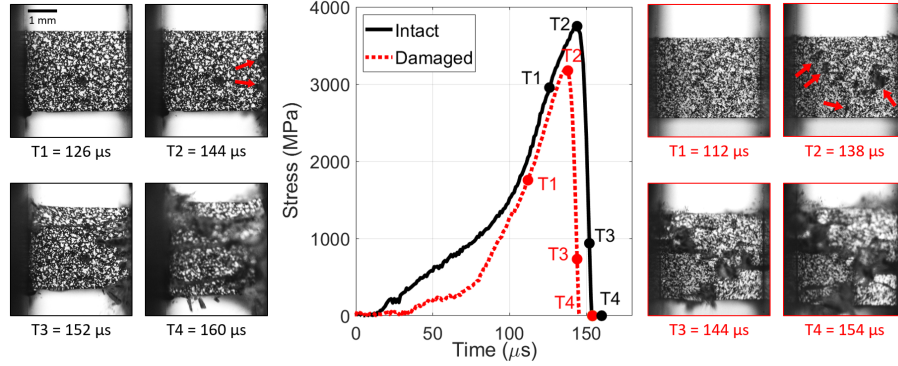


Figure 3.6: Stress-time histories of dynamic compression of intact (shown in black) and pre-damaged (shown in red) AD995 with high-speed video images showing failure process. Red arrows are used to indicate surface crack initiation points.

of $144\ \mu\text{s}$. The cracking spreads along the right edge of the specimen, and a large axial crack propagates along the top of the specimen. Note that at a time of $152\ \mu\text{s}$, the bottom left corner of the specimen still has not moved or cracked, indicating that part of the specimen is still load-bearing. Finally, at $160\ \mu\text{s}$, the specimen is fully fragmented and no longer bears any load. It can be seen that the fragments are long and oriented parallel to the loading direction, similar to the axial splitting observed for other advanced ceramics. This fracture behavior is consistent with the failure process observed in high-speed visualization of SPHB tests on other advanced ceramics (e.g., boron carbide [10, 116]).

For the damaged specimen, the initial surface damage develops in the middle of the specimen along pre-existing cracks rather than at the edges. Isolated cracks begin to grow simultaneously across the specimen surface at a time of $138\ \mu\text{s}$, then coalesce at $144\ \mu\text{s}$, leading to the failure of the specimen. At $154\ \mu\text{s}$, the specimen is fully fragmented. Unlike the axial cracks that dominate the fracture of the intact specimens, the damaged specimen shows a mix of inclined and axial cracking. The large inclined cracks are attributed to the opening of pre-existing cracks. Axial cracks can be observed in the top right and bottom left corners of the specimen at $154\ \mu\text{s}$, which only initiate after the major inclined cracks have coalesced at $144\ \mu\text{s}$. Axial splitting was also observed in the initially crack-free regions of damaged specimens in other

dynamic tests. Overall, the fragments observed at $154\ \mu\text{s}$ are larger for the pre-damaged specimens than for the intact specimens.

3.4 Discussion

This paper presents microstructural and mechanical characterization results on intact and damaged AD995 alumina, focusing on local deformation features and the effects of crack damage on mechanical response. To quantify the level of damage in pre-damaged specimens, XCT was applied to characterize the internal crack networks. The mechanical response of intact and pre-damaged specimens were then probed at quasi-static and dynamic rates. In the discussion section, we connect physical crack damage parameters to the degradation of mechanical properties in damaged ceramics, and then discuss the implications of the results in this paper in the context of ballistic response and computational modeling of material behavior.

3.4.1 Relationship Between Crack Orientation and Crack Closure

As noted in Section 3.3.2, the stiffness of the damaged specimens increase with crack closure up until a transition strain, at which point the majority of the cracks are closed and the stiffness stops increasing. Similar stiffening behaviors have been observed in excavated rocks[117], and past investigators have studied the stress threshold required to close cracks in brittle rocks[118, 119]. In this study we connect crack closure strains to XCT crack measurements. Based on the contour analysis in Section 3.3.3, cracks oriented between 0° and 40° with respect to the loading axis contribute most significantly to localized axial strains, as they coincide with the greatest localization of compressive axial strain. Beyond this range, localized axial strains decrease with increasing angle with respect to the loading axis, up to a maximum angle of approximately 60° , above which the inclined and vertical cracks experience similar axial strains to the undamaged parts of the specimen. Therefore, crack surfaces with orientations between 0° and 60° are believed to contribute most to the crack closure strain. To estimate the transition strain that signals the

effective closure of pre-existing cracks, we applied a moving window regression approach[118] to compute the stiffness of the damaged specimens and defined the transition strain as the first point at which the stiffness stabilizes at a constant value. This axial strain typically also marks the point at which the lateral strain linearizes. The estimated transition strains for the damaged specimens are plotted on Figure 3.7 as a function of the crack surface area for orientations between 0° and 60° for each specimen. Overall, it can be seen that the transition strain increases with increasing low-angle crack area, with the exception of few dynamic tests. For the two dynamic tests with the lowest crack surface area (DYN D1 and DYN D2), the transition strains are higher than expected when compared to the quasi-static tests with similar crack area (QS D1 and QS D2). The dynamic test with the greatest damage, DYN D4, also shows a much lower transition strain than expected. Despite significant differences in crack surface area, DYN D4 has a transition strain similar to that of DYN D3. Deviations from the trend of increasing crack closure strain with increasing low-angle crack area may be attributed to variations in crack thicknesses and loading rates. In comparing the crack surface orientation to the transition strain, we assume that the cracks are of similar thicknesses across different orientations for different specimens. However, it is possible, for example, that some specimens have fewer low-angle cracks with greater thicknesses while other specimens have more low-angle cracks that are thinner or closed. In these cases, the specimen with the fewer, but thicker, cracks may experience a greater closure strain. Therefore, a certain level of scatter is to be expected. As well, under quasi-static compression, the crack surfaces have time to slide and shift past asperities for maximum closure, but under dynamic compression, the load is applied so quickly that the cracks may not have enough time to close completely before failure starts. Consequently, the scatter in transition strain is expected to be greater for the dynamic regime than for the quasi-static regime.

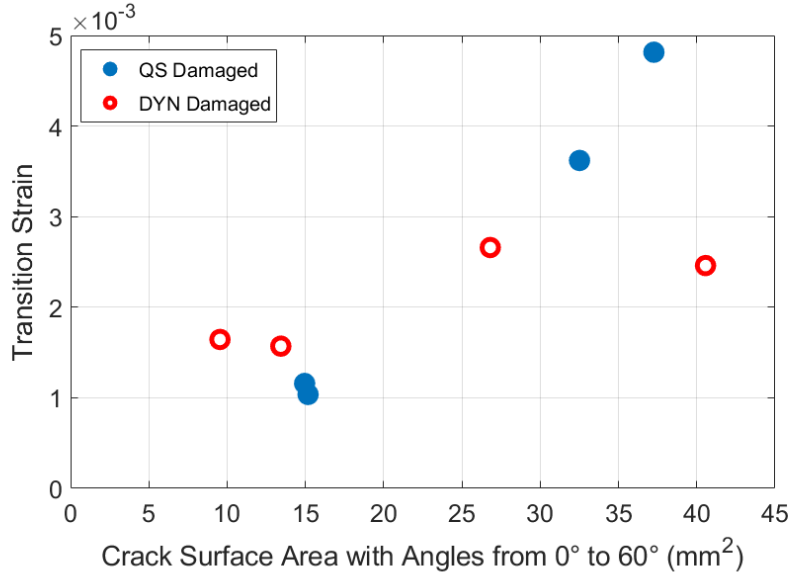


Figure 3.7: Transition strain plotted as a function of the crack surface area for orientations between 0° and 60° for each specimen. Blue points represent quasi-static results and red points represent dynamic results.

3.4.2 Relationship Between Crack Surface Area and Strength

The quasi-static and dynamic strength results are plotted against XCT crack surface area measurements in Figure 3.8. Across the range of crack damage accessed, there is no clear relationship between crack surface area and quasi-static strength. The weakest specimen tested in quasi-static compression, QS D1, has the lowest crack surface area, while the strength of the other damaged specimens are within the scatter of intact quasi-static strength measurements. From the contour plot in Figure 3.4A, it is clear that the opening of the axial crack causes QS D1 to fail. This suggests that the extent of overall crack damage is not as critical for quasi-static compression. Instead, fracture is likely governed by the most deleterious crack, which would lead to more stochastic results in the quasi-static regime, as is commonly assumed in the literature. As noted in Section 3.3.3, even though both specimens QS D1 and QS D3 both have large axial cracks, the effects of the axial cracks on the mechanical response are dramatically different for the two specimens. Alternatively, if the transition from intact to failed material is instantaneous, as

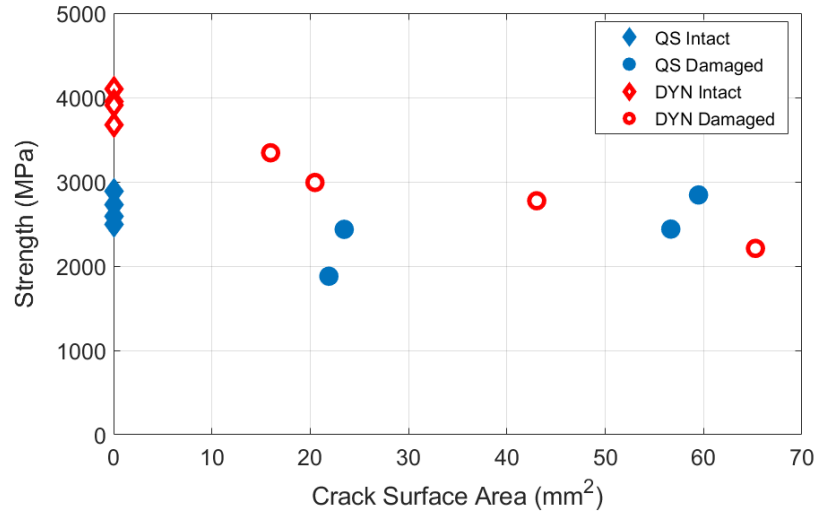


Figure 3.8: Compressive strength is plotted as a function of total crack surface area. Blue points represent quasi-static results and red points represent dynamic results. Diamonds indicate intact results and circles indicate damaged results.

assumed by the JH-1 model[120], then it is possible that the range of damage accessed in this study did not reach the transition point. More data is required to determine the relationship between crack damage and quasi-static strength.

In contrast, the dynamic experiments show decreasing strength with increasing crack surface area over the damage levels accessed in this study. This trend is consistent with the JH-2 model[6] assumption that the transition from intact to failed material is gradual. From the dynamic experiments, it was found that the damaged specimens exhibited a greater rate of lateral expansion than the intact specimens. This suggests that the presence of pre-existing cracks leads to an increased rate of damage development, as lateral expansion is interpreted to be the consequence of crack growth[121]. In addition, the rate of lateral expansion for damaged specimens was found to be greater at dynamic strain rates than at quasi-static strain rates, which indicates that crack growth is more sensitive to pre-existing damage in dynamic compression. Note also that four of the five damaged specimens tested in dynamic compression have strength values comparable to, if not higher than, the intact specimens tested in quasi-static compression, showing that the damaged

specimens still exhibit rate-dependent strength. With increasing damage, the dynamic strength of the damaged specimens eventually fall below those of the quasi-static results for comparable damage levels. This suggests that, while there is a rate-dependent increase in the strength of damaged specimens, the rate-dependence decreases with increasing damage. The rate strengthening effect in ceramics is thought to be related to the increased nucleation of new cracks in intact material[3, 8, 75]. Therefore, with increasing damage, the energy required to nucleate new cracks likely supersedes the energy required to grow pre-existing cracks. In the damaged specimens, high-speed visualization of the dynamic failure process also showed that the solid regions, free of pre-existing cracks, sometimes exhibited axial splitting. We believe this is caused by the nucleation of new cracks in the relatively undamaged regions, which eventually coalesce to form axial cracks. At the same time, the regions of the specimen with greater local crack damage are expected to fracture along preferentially oriented pre-existing cracks. This suggests that the rate effect may be related to the amount of crack-free volume within the damaged specimens.

In a similar study by Krinsky et al.[99], damaged boron carbide was found to be stronger under quasi-static compression than dynamic compression for similar levels of damage, as quantified by crack surface area. It is possible that the extent of pre-existing cracks for those specimens exceeded the threshold for which the rate effect is no longer active; thus, the strength is comparable at both rates. Furthermore, under quasi-static compression, the damaged specimens in that study experienced significant strength reductions in comparison to the intact specimens, indicating a high degree of damage. Note that the range of internal crack surface area probed in the present study and by Krinsky et al.[99] are comparable, however, given the differences in microstructure between the materials investigated in these studies (i.e., boron carbide in Krinsky et al.[99], and alumina in this study), the same level of crack damage is not expected to have the same effect on mechanical behavior.

3.4.3 Ballistic Performance of Damaged Ceramics

In this section, we discuss the mechanical response of damaged ceramics in the context of ballistic performance. We have shown in this study that the primary effects of crack damage in ceramics are to reduce the initial stiffness, initial rate of lateral expansion, and strength under compressive loading. A high stiffness is thought to contribute to ballistic performance by extending the duration of the dwell phase[122] and producing larger fragments which are believed to be more effective at eroding projectiles[5]. For a damaged ceramic, the low initial stiffness is expected to significantly degrade the dwell effect during a ballistic impact and may also lead to increased bending of the ceramic tile, which can cause undesirable fragmentation modes[123]. The reduced initial rate of lateral expansion due to crack closure is also believed to be detrimental to ballistic performance as it effectively decreases the confining pressure from material expansion, and confinement has been shown to be an important factor for improving ballistic resistance[100, 124]. In the literature, the effects of compressive strength on ballistic performance have been more controversial. Some studies have correlated increased compressive strength to improved penetration resistance[125, 126] while others have assigned it a more minor role in determining ballistic performance[5, 127].

These observations motivate armor designs that incorporate greater confining pre-stress[128–130]. Increased axial and lateral confining pressure can serve to close up major cracks that form following an impact, allowing the ceramic to recover its intact stiffness and retain lateral confinement. In one study, Anderson et al.[86] conducted long rod penetration experiments on intact and pre-damaged silicon carbide targets confined in aluminum sleeves and found negligible differences in penetration velocities between intact and damaged targets. In addition, Horsfall and Buckley[131] conducted ballistic experiments on alumina tiles with large through-thickness cracks and found that the ballistic limit velocity was lowered by only 3%. In their experimental setup, the alumina tile was confined by a composite backing and a frontal spall shield. The small differences in performance between damaged and intact ce-

ramics in these studies may be attributed to the confining pre-stress closing over cracks in the damaged specimens. Taken together, these results suggest that confinement is key to improving the durability and multi-hit capability of ceramic armors.

3.4.4 Computational Models for Ballistic Impacts

To simulate ballistic impacts on ceramics, it is necessary to account for the damaged state of ceramics. For instance, in the Rajendran-Grove micro-mechanics based impact model[7, 132–134], damage is tracked by increasing micro-crack density, and stiffness degrades as the material becomes progressively damaged. In the JH-1[120] and JH-2 models[6], both phenomenological models, damaged is defined as accumulated plastic strain, and the material strength degrades as the material transitions from intact to failed. The relationships between damage variables and degradation of mechanical properties are central to generating accurate predictions in impact models, as past investigators have emphasized[83, 135–138]. However, little work has been done to experimentally connect physical measures of damage parameters to the degradation of mechanical properties[99]. In this study, we seek to fill this gap by providing quantitative characterization of the local and global strains related to the crack structures. Deformation mechanisms, including crack closure, expansion into existing cracks, and crack sliding, and their connections to the evolution of mechanical properties in damaged ceramics have been highlighted in this paper to elucidate the behavior of damaged ceramics and guide future model development. In addition, the qualitative observations of the differences in failure process for intact and damaged ceramics can also be used to validate model outputs. As an example, consider the damage models in the JH-1 model[120], which treats the transition from intact to failed as instantaneous, and the JH-2 model[6], which was later developed to account for a gradual transition from intact to failed. The strength results from this study suggest that the transition is gradual at dynamic strain rates, but may be instantaneous at quasi-static strain rates.

3.5 Conclusion

Computational modeling of ballistic events is key to the development of advanced ceramic armor systems. This requires a clear understanding of the behavior of damaged ceramics. In this study, we investigated the effects of damage on the mechanical behavior of alumina, focusing on the connections between physical crack damage parameters and the degradation of mechanical properties. XCT was used to quantify internal crack networks, and DIC was used to characterize mechanical response. We visualized the local deformation mechanisms related to crack damage, including crack closure, opening, and sliding, and highlighted their connections to the evolution of global stress-strain behaviors in damaged ceramics. Lastly, high-speed photography was used to visualize the difference in fracture behavior between intact and damaged alumina. Altogether, the results generated in this study expand our understanding of damaged ceramics and support future model development.

3.6 Acknowledgment

This research was sponsored by the Army Research Laboratory and was accomplished under Cooperative Agreement Number W91NF-16-2-0079 and W911NF-17-2-0213. The views and conclusions contained in this document are those of the authors and should not be interpreted as representing the official policies, either expressed or implied, of the Army Research Laboratory or the U.S. Government. The U.S. Government is authorized to reproduce and distribute reprints for Government purposes notwithstanding any copyright notation herein. The authors would also like to express their thanks to Bernie Faulkner, Rick Bubenko, Haoyang Li, and Kapil Bhagavathula for their help in conducting the experiments.

Research described in this paper was performed at the BMIT facility at the Canadian Light Source, which is supported by the Canada Foundation for Innovation, Natural Sciences and Engineering Research Council of Canada, the University of Saskatchewan, the Government of Saskatchewan, Western

Economic Diversification Canada, the National Research Council Canada, and the Canadian Institutes of Health Research. We acknowledge Sergei Gasilov and Ning Zhu for their help in obtaining and reconstructing the XCT scans.

Chapter 4

Concluding Remarks

4.1 Implications

This thesis explored the characterization of intact and damaged aluminum oxide, focusing on connections between microstructural features and strain rate dependent mechanical behavior. XCT was applied to visualize processing-induced pores and internal crack networks in alumina microstructure. To reconstruct the XCT scans and generate quantitative characterization data, MATLAB software was developed, taking into consideration the unique requirements of different microstructural features. After microstructural characterization, quasi-static and dynamic compression experiments were performed to characterize the material behavior. This approach was used to study porous intact alumina and crack networks in damaged alumina. The main contributions of this thesis are summarized below:

1. An analysis framework for reconstructing and analyzing XCT scans has been developed to improve the three-dimensional characterization of microstructural features in ceramics. The quantitative characterization metrics incorporated into this framework can be used to optimize the design of new materials and aid in quality control in manufacturing. This methodology is also applicable to other materials with pores or secondary phase particles (e.g., foams, composites, and 3D printed parts).
2. This thesis presents improved microstructural and mechanical characterization data on intact and damaged alumina. The three-dimensional

defect data, serving as model input parameters, improves the fidelity of material models, and the stress-strain curves are useful for validating model predictions.

3. The characterization of damaged alumina in this work contributes to our understanding of the effects of crack damage on advanced ceramics and informs the development of future damage models[6]. Damage is commonly modeled as a homogeneous degradation of elastic properties in the literature. This work has shown that crack damage in ceramics can lead to a complex evolution of mechanical properties, cause localized strains to develop, and modify the fracture process.

4.2 Future Work

Possible research directions for extending the work in this thesis are outlined below:

- *Improving XCT characterization* - In the current framework, only inhomogeneities with convex, ellipsoidal shapes may be accurately represented. To improve the applicability of XCT characterization in materials, defect representation should be extended to account for other types of inhomogeneities (e.g., concave cracks). This may be accomplished by fitting other shapes to the segmented inhomogeneity.
- *Studying process-structure-property relationships* - The XCT characterization metrics developed for defect populations in intact alumina may be applied to materials where the processing is known or controlled in order to study the effects of varying processing parameters on the resulting microstructure (e.g., spatial distribution of inhomogeneities) and its attendant effects on mechanical properties (e.g., strength).
- *Exploring different types of crack damage* - In this study, XCT was used to analyze macroscopic cracks that were on the scale of the specimen, but the same approach can also be used to characterize micro-cracks in brittle materials, which can be applied to validate the physical mechanisms

in micromechanical models. Rather than using thermal shock cycles to induce damage, mechanical load-unload cycles may produce cracks that are more representative of the damage encountered during compressive loading. Alternatively, 3D printing may offer a another way to control the crack characteristics. By 3D printing ceramics with pre-defined cracks with known characteristics, critical micro-crack orientations and sizes may be isolated and explored experimentally.

- *Further investigations into the behavior of damaged materials* - In this thesis, and past studies on damaged ceramics[91, 92, 99], mechanical testing have been limited to the compressive stress state at strain rates ranging from 10^{-3} to $10^3 s^{-1}$. Following the approach outlined in , the behavior of damaged ceramics may be explored further under different stress-states (e.g., shear and tension) and for intermediate and higher strain rates (e.g., shock compression).

References

- [1] B Matchen. “Applications of ceramics in armor products.” In: *Key Engineering Materials*. Vol. 122. Trans Tech Publ. 1996, pp. 333–344. 1
- [2] Donald A Shockey et al. “Failure phenomenology of confined ceramic targets and impacting rods.” In: *International Journal of Impact Engineering* 9.3 (1990), pp. 263–275. 1, 38
- [3] James Lankford Jr. “The Role of Dynamic Material Properties in the Performance of Ceramic Armor.” In: *International Journal of Applied Ceramic Technology* 1.3 (2004), pp. 205–210. 1, 33, 63
- [4] Weinong W. Chen et al. “Dynamic Fracture of Ceramics in Armor Applications.” In: *Journal of the American Ceramic Society* 90.4 (2007), pp. 1005–1018. 1, 7, 83
- [5] Andreas Krell and Elmar Strassburger. “Order of influences on the ballistic resistance of armor ceramics and single crystals.” In: *Materials Science and Engineering: A* 597 (2014), pp. 422–430. 1, 64
- [6] Gordon R Johnson and Tim J Holmquist. “An improved computational constitutive model for brittle materials.” In: *AIP conference proceedings*. Vol. 309. 1. AIP. 1994, pp. 981–984. 1, 62, 65, 69
- [7] AM Rajendran. “Modeling the impact behavior of AD85 ceramic under multiaxial loading.” In: *International Journal of Impact Engineering* 15.6 (1994), pp. 749–768. 1, 65
- [8] B. Paliwal and K.T. Ramesh. “An interacting micro-crack damage model for failure of brittle materials under compression.” In: *Journal of the Mechanics and Physics of Solids* 56.3 (2008), pp. 896–923. 1, 31, 34, 44, 63
- [9] B. Wattrisse et al. “Analysis of strain localization during tensile tests by digital image correlation.” In: *Experimental Mechanics* 41.1 (Mar. 2001), pp. 29–39. 1, 19, 46
- [10] James D Hogan et al. “The effects of microstructure and confinement on the compressive fragmentation of an advanced ceramic.” In: *Journal of the American Ceramic Society* 98.3 (2015), pp. 902–912. 1, 58

- [11] Calvin Lo, Tomoko Sano, and James D. Hogan. “Microstructural and Mechanical Characterization of Variability in Porous Advanced Ceramics using X-ray Computed Tomography and Digital Image Correlation.” In: *Materials Characterization* (2019), p. 109929. 3, 39, 42
- [12] Calvin Lo, Tomoko Sano, and James D Hogan. “Deformation Mechanisms and Evolution of Mechanical Properties in Damaged Advanced Ceramics.” In: *Journal of the European Ceramic Society* (2020). 4
- [13] S.-T. Buljan and S.F. Wayne. “Wear and design of ceramic cutting tool materials.” In: *Wear* 133.2 (1989), pp. 309–321. 7
- [14] Laurent SEDEL. “Evolution of alumina-on-alumina implants: A review.” In: *Clinical orthopaedics and related research* 379 (2000), pp. 48–54. 7
- [15] June-Ho Park et al. “Densification and Mechanical Properties of Titanium Diboride with Silicon Nitride as a Sintering Aid.” In: *Journal of the American Ceramic Society* 82.11 (1999), pp. 3037–3042. 7
- [16] Roy Arrowood and James Lankford. “Compressive fracture processes in an alumina-glass composite.” In: *Journal of Materials Science* 22.10 (Oct. 1987), pp. 3737–3744. 7, 15, 28
- [17] R. L. COBLE and W. D. KINGERY. “Effect of Porosity on Physical Properties of Sintered Alumina.” In: *Journal of the American Ceramic Society* 39.11 (1956), pp. 377–385. 7
- [18] James David Hogan et al. “The effects of defects on the uniaxial compressive strength and failure of an advanced ceramic.” In: *Acta Materialia* 102 (2016), pp. 263–272. 7, 13, 15
- [19] S. C. CARNIGLIA. “Working Model for Porosity Effects on the Uniaxial Strength of Ceramics.” In: *Journal of the American Ceramic Society* 55.12 (1972), pp. 610–618. 7, 13
- [20] N. Ramakrishnan and V. S. Arunachalam. “Effective Elastic Moduli of Porous Ceramic Materials.” In: *Journal of the American Ceramic Society* 76.11 (1993), pp. 2745–2752. 7
- [21] Guangli Hu et al. “A 3D mechanistic model for brittle materials containing evolving flaw distributions under dynamic multiaxial loading.” In: *Journal of the Mechanics and Physics of Solids* 78 (2015), pp. 269–297. 7
- [22] Nitin P. Daphalapurkar et al. “Predicting variability in the dynamic failure strength of brittle materials considering pre-existing flaws.” In: *Journal of the Mechanics and Physics of Solids* 59.2 (2011), pp. 297–319. 7
- [23] S. Levy and J.F. Molinari. “Dynamic fragmentation of ceramics, signature of defects and scaling of fragment sizes.” In: *Journal of the Mechanics and Physics of Solids* 58.1 (2010), pp. 12–26. 7, 31

- [24] Hiroya Abe et al. “Flaw Size Distribution in High-Quality Alumina.” In: *Journal of the American Ceramic Society* 86.6 (2003), pp. 1019–1021. 7, 12, 21
- [25] Nobuhiro Shinohara et al. “Morphological Changes in Process-Related Large Pores of Granular Compacted and Sintered Alumina.” In: *Journal of the American Ceramic Society* 83.7 (2000), pp. 1633–1640. 7
- [26] Yao Zhang et al. “Characterization of processing pores and their relevance to the strength in alumina ceramics.” In: *Journal of Materials Research* 14.8 (1999), pp. 3370–3374. 7, 12
- [27] Carli A. Moorehead, Jennifer M. Sietins, and Jeffrey J. Swab. “Meso-scale microstructural agglomerate quantification in boron carbide using X-ray microcomputed tomography.” In: *Materials Characterization* 141 (2018), pp. 177–185. 8, 30
- [28] J. Nafar Dastgerdi et al. “Multiscale microstructural characterization of particulate-reinforced composite with non-destructive X-ray micro- and nanotomography.” In: *Composite Structures* 194 (2018), pp. 292–301. 8
- [29] S. Tammam-Williams et al. “XCT analysis of the influence of melt strategies on defect population in Ti–6Al–4V components manufactured by Selective Electron Beam Melting.” In: *Materials Characterization* 102 (2015), pp. 47–61. 8, 12, 14, 30
- [30] M Li et al. “Three dimensional characterization and modeling of particle reinforced metal matrix composites: part I: Quantitative description of microstructural morphology.” In: *Materials Science and Engineering: A* 265.1 (1999), pp. 153–173. 8, 16, 17
- [31] M. Li et al. “Three dimensional characterization and modeling of particle reinforced metal matrix composites part II: damage characterization.” In: *Materials Science and Engineering: A* 266.1 (1999), pp. 221–240. 8, 17
- [32] Lori Graham-Brady. “Statistical characterization of meso-scale uniaxial compressive strength in brittle materials with randomly occurring flaws.” In: *International Journal of Solids and Structures* 47.18 (2010), pp. 2398–2413. 8, 15, 31
- [33] Coorstek. *Advanced alumina brochure*. Brochure. 2016. 8, 9
- [34] Tomoko Sano et al. “Correlation of Microstructure to Mechanical Properties in Two Grades of Alumina.” In: *Characterization of Minerals, Metals, and Materials 2018*. Ed. by Bowen Li et al. Cham: Springer International Publishing, 2018, pp. 75–81. 9, 30, 40

- [35] Tomasz W. Wysokinski et al. “Beamlines of the biomedical imaging and therapy facility at the Canadian light source—Part 1.” In: *Nuclear Instruments and Methods in Physics Research Section A: Accelerators, Spectrometers, Detectors and Associated Equipment* 582.1 (2007). Proceedings of the 14th National Conference on Synchrotron Radiation Research, pp. 73–76. 10
- [36] Kanti V. Mardia and TJ Hainsworth. “A spatial thresholding method for image segmentation.” In: *IEEE transactions on pattern analysis and machine intelligence* 10.6 (1988), pp. 919–927. 11, 42
- [37] E. Maire and P. J. Withers. “Quantitative X-ray tomography.” In: *International Materials Reviews* 59.1 (2014), pp. 1–43. 12
- [38] S. R. Stock. “Recent advances in X-ray microtomography applied to materials.” In: *International Materials Reviews* 53.3 (2008), pp. 129–181. 12, 14
- [39] H Horii and S Nemat-Nasser. “Compression-induced microcrack growth in brittle solids: Axial splitting and shear failure.” In: *Journal of Geophysical Research: Solid Earth* 90.B4 (1985), pp. 3105–3125. 12, 44, 55
- [40] M Kachanov, I Tsukrov, and B1 Shafiro. “Effective moduli of solids with cavities of various shapes.” In: *Applied Mechanics Reviews* 47.1S (1994), S151–S174. 13
- [41] Anthony P Roberts and Edward J Garboczi. “Elastic properties of model porous ceramics.” In: *Journal of the American Ceramic Society* 83.12 (2000), pp. 3041–3048. 13
- [42] Giovanni Bruno and Mark Kachanov. “Microstructure–property connections for porous ceramics: the possibilities offered by micromechanics.” In: *Journal of the American Ceramic Society* 99.12 (2016), pp. 3829–3852. 13
- [43] TE Mitchell, KPD Lagerlöf, and AH Heuer. “Dislocations in ceramics.” In: *Materials science and technology* 1.11 (1985), pp. 944–949. 14
- [44] HP Iwata et al. “Stacking faults in silicon carbide.” In: *Physica B: Condensed Matter* 340 (2003), pp. 165–170. 14
- [45] Anze Shui, Nozomu Uchida, and Keizo Uematsu. “Origin of shrinkage anisotropy during sintering for uniaxially pressed alumina compacts.” In: *Powder Technology* 127.1 (2002), pp. 9–18. 14, 24
- [46] Anze Shui et al. “Development of anisotropic microstructure in uniaxially pressed alumina compacts.” In: *Journal of the European Ceramic Society* 22.8 (2002), pp. 1217–1223. 14, 24
- [47] A. Zavaliangos, J. M. Missiaen, and D. Bouvard. “Anisotropy in shrinkage during sintering.” In: *Science of Sintering* 38.1 (2006), pp. 13–25. 14

- [48] H. P. KIRCHNER and R. M. GRUVER. “Strength-Anisotropy-Grain Size Relations in Ceramic Oxides.” In: *Journal of the American Ceramic Society* 53.5 (1970), pp. 232–236. 14
- [49] H. F. Fischmeister. “Applications of quantitative microscopy in materials engineering.” In: *Journal of Microscopy* 95.1 (1972), pp. 119–143. 14
- [50] W.A. Spitzig, J.F. Kelly, and O. Richmond. “Quantitative characterization of second-phase populations.” In: *Metallography* 18.3 (1985), pp. 235–261. 14, 16, 17
- [51] S. Nemat-Nasser and H. Deng. “Strain-rate effect on brittle failure in compression.” In: *Acta Metallurgica et Materialia* 42.3 (1994), pp. 1013–1024. 15
- [52] Fenghua Zhou, Jean-François Molinari, and K.T. Ramesh. “A cohesive model based fragmentation analysis: effects of strain rate and initial defects distribution.” In: *International Journal of Solids and Structures* 42.18 (2005), pp. 5181–5207. 15
- [53] R.A. Dorey, J.A. Yeomans, and P.A. Smith. “Effect of pore clustering on the mechanical properties of ceramics.” In: *Journal of the European Ceramic Society* 22.4 (2002), pp. 403–409. 15
- [54] Ryszard Pyrz. “Quantitative description of the microstructure of composites. Part I: Morphology of unidirectional composite systems.” In: *Composites Science and Technology* 50.2 (1994), pp. 197–208. 16, 17
- [55] P.P. Bansal and A.J. Ardell. “Average nearest-neighbor distances between uniformly distributed finite particles.” In: *Metallography* 5.2 (1972), pp. 97–111. 16, 17
- [56] N. Yang et al. “Simulation and quantitative assessment of finitesize particle distributions in metal matrix composites.” In: *Materials Science and Technology* 16.7-8 (2000), pp. 797–805. 17
- [57] Michele Cappellari and Yannick Copin. “Adaptive spatial binning of integral-field spectroscopic data using Voronoi tessellations.” In: *Monthly Notices of the Royal Astronomical Society* 342.2 (June 2003), pp. 345–354. 17
- [58] Anne Poupon. “Voronoi and Voronoi-related tessellations in studies of protein structure and interaction.” In: *Current Opinion in Structural Biology* 14.2 (2004), pp. 233–241. 17
- [59] N. C. Kenkel. “Spatial Competition Models for Plant Populations.” In: *Computer assisted vegetation analysis*. Ed. by E. Feoli and L. Orlóci. Dordrecht: Springer Netherlands, 1991, pp. 387–397. 17
- [60] Jean-Noël Périé et al. “Analysis of a multiaxial test on a C/C composite by using digital image correlation and a damage model.” In: *Experimental Mechanics* 42.3 (Sept. 2002), pp. 318–328. 19, 46

- [61] A-F. Bastawros, H. Bart-Smith, and A.G. Evans. “Experimental analysis of deformation mechanisms in a closed-cell aluminum alloy foam.” In: *Journal of the Mechanics and Physics of Solids* 48.2 (2000), pp. 301–322. 19, 46
- [62] Bing Pan et al. “Two-dimensional digital image correlation for in-plane displacement and strain measurement: a review.” In: *Measurement Science and Technology* 20.6 (2009), p. 062001. 19, 46
- [63] Y.L. Dong and B. Pan. “A Review of Speckle Pattern Fabrication and Assessment for Digital Image Correlation.” In: *Experimental Mechanics* 57.8 (Oct. 2017), pp. 1161–1181. 19, 46
- [64] Hubert W Schreier, Joachim R Braasch, and Michael A Sutton. “Systematic errors in digital image correlation caused by intensity interpolation.” In: *Optical engineering* 39 (2000). 20, 46
- [65] Satoshi Nakamura et al. “Strength-Processing Defects Relationship Based on Micrographic Analysis and Fracture Mechanics in Alumina Ceramics.” In: *Journal of the American Ceramic Society* 92.3 (2009), pp. 688–693. 21
- [66] L.-S. Chang, T.-H. Chuang, and W.J. Wei. “Characterization of alumina ceramics by ultrasonic testing.” In: *Materials Characterization* 45.3 (2000), pp. 221–226. 24
- [67] Wu, X. J. and Gorham, D. A. “Stress Equilibrium in the Split Hopkinson Pressure Bar Test.” In: *J. Phys. IV France* 07 (1997), pp. C3-91-C3-96. 26
- [68] J. Lankford. “Mechanisms Responsible for Strain-Rate-Dependent Compressive Strength in Ceramic Materials.” In: *Journal of the American Ceramic Society* 64.2 (1981), C-33-C-34. 28, 49
- [69] J. Lankford. “High strain rate compression and plastic flow of ceramics.” In: *Journal of Materials Science Letters* 15.9 (Jan. 1996), pp. 745–750. 28
- [70] K. L. Gavrilov et al. “Role of magnesia and silica in alumina microstructure evolution.” In: *Journal of Materials Science* 38.19 (Oct. 2003), pp. 3965–3972. 30, 31
- [71] M. Adams and G. Sines. “Methods for Determining the Strength of Brittle Materials in Compressive Stress States.” In: (1976). 33
- [72] Jeffrey J. Swab et al. “Static and dynamic compression strength of hot-pressed boron carbide using a dumbbell-shaped specimen.” In: *Journal of Materials Science* 52.17 (Sept. 2017), pp. 10073–10084. 33
- [73] Waloddi Weibull. “A statistical theory of strength of materials.” In: *Royal Swedish Institute for Engineering Research* (1939), pp. 1–45. 33

- [74] Waloddi Weibull et al. “A statistical distribution function of wide applicability.” In: *Journal of applied mechanics* 18.3 (1951), pp. 293–297. 33
- [75] K. Ravi-Chandar and W. G. Knauss. “An experimental investigation into dynamic fracture: III. On steady-state crack propagation and crack branching.” In: *International Journal of Fracture* 26.2 (Oct. 1984), pp. 141–154. 33, 63
- [76] B. Paliwal and K.T. Ramesh. “Effect of crack growth dynamics on the rate-sensitive behavior of hot-pressed boron carbide.” In: *Scripta Materialia* 57.6 (2007), pp. 481–484. 34
- [77] MB Mukasey, Jeffrey L Sedgwick, and DW Hagy. “Ballistic Resistance of Body Armor, NIJ Standard-0101.06.” In: *US Department of Justice (www.ojp.usdoj.gov/nij)* (2008). 38
- [78] E Strassburger and H Senf. *Experimental Investigations of Wave and Fracture Phenomena in Impacted Ceramics and Glasses*. Tech. rep. FRAUNHOFER-INST FUER KURZZEITDYNAMIK-ERNST-MACH-INST WEIL AM RHEIN (GERMANY), 1995. 38
- [79] Neil Bourne, Jeremy Millett, and Zvi Rosenberg. “On the origin of failure waves in glass.” In: *Journal of applied physics* 81.10 (1997), pp. 6670–6674. 38
- [80] NK Bourne. “On the impact and penetration of soda-lime glass.” In: *International journal of impact engineering* 32.1-4 (2005), pp. 65–79. 38
- [81] Yehuda Partom. “Modeling failure waves in glass.” In: *International journal of impact engineering* 21.9 (1998), pp. 791–799. 38
- [82] Th Behner et al. “Penetration and failure of lead and borosilicate glass against rod impact.” In: *International Journal of Impact Engineering* 35.6 (2008), pp. 447–456. 38
- [83] Timothy J Holmquist. “Some observations on the strength of failed ceramic.” In: *Advances in Ceramic Armor: A Collection of Papers Presented at the 29th International Conference on Advanced Ceramics and Composites, Jan 23-28, 2005, Cocoa Beach, FL*. Vol. 296. John Wiley & Sons. 2009, p. 3. 38, 65
- [84] TJ Holmquist. “Analysis of the response of silicon carbide subjected to shock-res shock and shock-release plate-impact experiments.” In: *Journal de Physique IV (Proceedings)*. Vol. 134. EDP sciences. 2006, pp. 339–344. 38
- [85] Charles E Anderson Jr et al. “Time-resolved penetration into pre-damaged hot-pressed silicon carbide.” In: *International Journal of Impact Engineering* 35.8 (2008), pp. 661–673. 38

- [86] Charles Anderson Jr et al. *Long-rod penetration into intact and pre-damaged SiC ceramic*. Tech. rep. SOUTHWEST RESEARCH INST SAN ANTONIO TX, 2008. 38, 64
- [87] Kathryn A Dannemann et al. “Response and characterization of confined borosilicate glass: Intact and damaged.” In: *Advances in ceramic armor II, a collection of papers presented at the 30th int. conf. & exp. on advanced ceramics and composites*. Vol. 27. 7. 2006, 119e29. 38
- [88] Sidney Chocron et al. “Intact and predamaged boron carbide strength under moderate confinement pressures.” In: *Journal of the American Ceramic Society* 95.1 (2012), pp. 350–357. 38
- [89] Charles E Anderson Jr. “Compression testing and response of SiC-N ceramics: intact, damaged and powder.” In: *Advances in Ceramic Armor: A Collection of Papers Presented at the 29th International Conference on Advanced Ceramics and Composites, Jan 23-28, 2005, Cocoa Beach, FL*. Vol. 296. John Wiley & Sons. 2009, p. 109. 38
- [90] Kathryn A Dannemann et al. “Compressive damage development in confined borosilicate glass.” In: *Materials Science and Engineering: A* 478.1-2 (2008), pp. 340–350. 38
- [91] Kathryn A Dannemann et al. “Damage development in confined borosilicate and soda-lime glasses.” In: *Journal of the American Ceramic Society* 95.2 (2012), pp. 721–729. 38, 70
- [92] Sidney Chocron et al. “Characterization of confined intact and damaged borosilicate glass.” In: *Journal of the American Ceramic Society* 93.10 (2010), pp. 3390–3398. 38, 70
- [93] S Chocron et al. “Pressure effects on the compressive response of confined intact and damaged soda-lime glass.” In: *Experimental Mechanics* 53.1 (2013), pp. 77–89. 38
- [94] Anna K Zurek and Dennis A Hunter. “Dynamic testing and characterization of pre-fractured ceramic.” In: *AIP Conference Proceedings*. Vol. 309. 1. AIP. 1994, pp. 761–764. 38
- [95] W Chen and H Luo. “Dynamic compressive responses of intact and damaged ceramics from a single split Hopkinson pressure bar experiment.” In: *Experimental mechanics* 44.3 (2004), pp. 295–299. 39
- [96] Huiyang Luo and Weinong Chen. “Dynamic compressive response of intact and damaged AD995 alumina.” In: *International Journal of Applied Ceramic Technology* 1.3 (2004), pp. 254–260. 39
- [97] Huiyang Luo, Weinong W Chen, and AM Rajendran. “Dynamic compressive response of damaged and interlocked SiC–N ceramics.” In: *Journal of the American Ceramic Society* 89.1 (2006), pp. 266–273. 39

- [98] Eric N Landis. “Toward a physical damage variable for concrete.” In: *Journal of engineering mechanics* 132.7 (2006), pp. 771–774. 39, 43
- [99] Erez Krinsky et al. “Quantification of damage and its effects on the compressive strength of an advanced ceramic.” In: *Engineering Fracture Mechanics* 208 (2019), pp. 107–118. 39, 63, 65, 70
- [100] Charles E Anderson Jr and Suzanne A Royal-Timmons. “Ballistic performance of confined 99.5%-Al₂O₃ ceramic tiles.” In: *International journal of impact engineering* 19.8 (1997), pp. 703–713. 40, 64
- [101] James Lankford et al. “The role of plasticity as a limiting factor in the compressive failure of high strength ceramics.” In: *Mechanics of Materials* 29.3-4 (1998), pp. 205–218. 40
- [102] NK Bourne et al. “On the Hugoniot elastic limit in polycrystalline alumina.” In: *Journal of Applied Physics* 102.7 (2007), p. 073514. 40
- [103] Adam Thompson, Ian Maskery, and Richard K Leach. “X-ray computed tomography for additive manufacturing: a review.” In: *Measurement Science and Technology* 27.7 (2016), p. 072001. 41
- [104] Tomasz W Wysokinski et al. “Beamlines of the biomedical imaging and therapy facility at the Canadian Light Source-Part 2.” In: *Journal of Physics: Conference Series*. Vol. 425. 7. IOP Publishing. 2013, p. 072013. 41
- [105] Zhouping Wei, Sheldon Wiebe, and Dean Chapman. “Ring artifacts removal from synchrotron CT image slices.” In: *Journal of Instrumentation* 8.06 (2013), p. C06006. 41
- [106] Amar Khellaf, Azeddine Beghdadi, and Henri Dupoisot. “Entropic contrast enhancement.” In: *IEEE transactions on medical Imaging* 10.4 (1991), pp. 589–592. 42, 53
- [107] Jiang Hsieh et al. “Computed tomography: principles, design, artifacts, and recent advances.” In: SPIE Bellingham, WA. 2009. 42
- [108] Luc Vincent. “Morphological area openings and closings for grey-scale images.” In: *Shape in Picture*. Springer, 1994, pp. 197–208. 43
- [109] Tyler S Oesch, Eric N Landis, and Daniel A Kuchma. “Conventional concrete and UHPC performance–damage relationships identified using computed tomography.” In: *Journal of Engineering Mechanics* 142.12 (2016), p. 04016101. 43
- [110] Mark L Kachanov. “A microcrack model of rock inelasticity part I: Frictional sliding on microcracks.” In: *Mechanics of Materials* 1.1 (1982), pp. 19–27. 44
- [111] William E Lorensen and Harvey E Cline. “Marching cubes: A high resolution 3D surface construction algorithm.” In: *ACM siggraph computer graphics*. Vol. 21. 4. ACM. 1987, pp. 163–169. 44

- [112] Timothy S Newman and Hong Yi. “A survey of the marching cubes algorithm.” In: *Computers & Graphics* 30.5 (2006), pp. 854–879. 44
- [113] Bing Pan et al. “Two-dimensional digital image correlation for in-plane displacement and strain measurement: a review.” In: *Measurement science and technology* 20.6 (2009), p. 062001. 47
- [114] Lingtao Mao et al. “3D strain evolution in concrete using in situ X-ray computed tomography testing and digital volumetric speckle photography.” In: *Measurement* 133 (2019), pp. 456–467. 47
- [115] H Horii and S Nemat-Nasser. “Overall moduli of solids with microcracks: load-induced anisotropy.” In: *Journal of the Mechanics and Physics of Solids* 31.2 (1983), pp. 155–171. 55
- [116] B Paliwal and KT Ramesh. “Effect of crack growth dynamics on the rate-sensitive behavior of hot-pressed boron carbide.” In: *Scripta materialia* 57.6 (2007), pp. 481–484. 58
- [117] Michael L Batzle, Gene Simmons, and Robert W Siegfried. “Microcrack closure in rocks under stress: direct observation.” In: *Journal of Geophysical Research: Solid Earth* 85.B12 (1980), pp. 7072–7090. 59
- [118] Erik Brian Eberhardt. “Brittle rock fracture and progressive damage in uniaxial compression.” PhD thesis. University of Saskatchewan Saskatoon, 1998. 59, 60
- [119] S-H Chang and C-I Lee. “Estimation of cracking and damage mechanisms in rock under triaxial compression by moment tensor analysis of acoustic emission.” In: *International Journal of Rock Mechanics and Mining Sciences* 41.7 (2004), pp. 1069–1086. 59
- [120] GR Johnson and TJ Holmquist. “A computational constitutive model for brittle materials subjected to large strains, high strain rates and high pressures.” In: *Shock wave and high-strain-rate phenomena in materials* (1992), pp. 1075–1081. 62, 65
- [121] Hong Wang and KT Ramesh. “Dynamic strength and fragmentation of hot-pressed silicon carbide under uniaxial compression.” In: *Acta Materialia* 52.2 (2004), pp. 355–367. 62
- [122] Andreas Krell and Elmar Strassburger. “Hierarchy of Key Influences on the Ballistic Strength of Opaque and Transparent Armor.” In: *Advances in Ceramic Armor III: Ceramic and Engineering Science Proceedings, Volume 28, Issue 5*. John Wiley and Sons, Ltd, 2009, pp. 45–55. 64
- [123] Brian R Lawn and David B Marshall. “Nonlinear stress-strain curves for solids containing closed cracks with friction.” In: *Journal of the Mechanics and Physics of Solids* 46.1 (1998), pp. 85–113. 64
- [124] RL Woodward et al. “A study of fragmentation in the ballistic impact of ceramics.” In: *International Journal of Impact Engineering* 15.5 (1994), pp. 605–618. 64

- [125] Z Rozenberg and Y Yeshurun. “The relation between ballastic efficiency and compressive strength of ceramic tiles.” In: *International journal of impact engineering* 7.3 (1988), pp. 357–362. 64
- [126] Z Rosenberg et al. “On the main mechanisms for defeating AP projectiles, long rods and shaped charge jets.” In: *International journal of impact engineering* 36.4 (2009), pp. 588–596. 64
- [127] Raymond L Woodward. “A simple one-dimensional approach to modelling ceramic composite armour defeat.” In: *International Journal of Impact Engineering* 9.4 (1990), pp. 455–474. 64
- [128] DR Curran et al. “Micromechanical model for comminution and granular flow of brittle material under high strain rate application to penetration of ceramic targets.” In: *International Journal of Impact Engineering* 13.1 (1993), pp. 53–83. 64
- [129] Olof Andersson, Patrik Lundberg, and R Renstrom. “Influence of confinement on the transition velocity of silicon carbide.” In: *Proc. 23rd International Symposium on Ballistics, Tarragona, Spain, April. 2007*, pp. 16–20. 64
- [130] Runqiang Chi et al. “Pre-stress effect on confined ceramic armor ballistic performance.” In: *International Journal of Impact Engineering* 84 (2015), pp. 159–170. 64
- [131] I Horsfall and D Buckley. “The effect of through-thickness cracks on the ballistic performance of ceramic armour systems.” In: *International journal of impact engineering* 18.3 (1996), pp. 309–318. 64
- [132] AM Rajendran and DJ Grove. “Determination of Rajendran-Grove ceramic constitutive model constants.” In: *AIP Conference Proceedings*. Vol. 370. 1. AIP. 1996, pp. 539–542. 65
- [133] AM Rajendran and DJ Grove. “Modeling the shock response of silicon carbide, boron carbide and titanium diboride.” In: *International Journal of Impact Engineering* 18.6 (1996), pp. 611–631. 65
- [134] DJ Grove and AM Rajendran. “Overview of the Rajendran-Grove ceramic failure model.” In: *Ceramic transactions* 134 (2002), pp. 371–382. 65
- [135] Charles E Anderson Jr. “A review of computational ceramic armor modeling.” In: *Proceedings of the 30* (2007). 65
- [136] Andrew L Tonge and KT Ramesh. “Multi-scale defect interactions in high-rate brittle material failure. Part I: Model formulation and application to ALON.” In: *Journal of the Mechanics and Physics of Solids* 86 (2016), pp. 117–149. 65

- [137] Andrew L Tonge and KT Ramesh. “Multi-scale defect interactions in high-rate failure of brittle materials, Part II: Application to design of protection materials.” In: *Journal of the Mechanics and Physics of Solids* 86 (2016), pp. 237–258. 65
- [138] SA Dyachkov et al. “Explicit failure model for boron carbide ceramics under shock loading.” In: *Journal of Applied Physics* 124.8 (2018), p. 085902. 65
- [139] Kapil Bharadwaj Bhagavathula et al. “High rate compressive behaviour of a dilatant polymeric foam.” In: *Journal of Dynamic Behavior of Materials* 4.4 (2018), pp. 573–585. 83
- [140] W Chen et al. “Dynamic small strain measurements of a metal specimen with a split Hopkinson pressure bar.” In: *Experimental Mechanics* 43.1 (2003), pp. 20–23. 83
- [141] Hoon Huh, WJ Kang, and SS Han. “A tension split Hopkinson bar for investigating the dynamic behavior of sheet metals.” In: *Experimental mechanics* 42.1 (2002), pp. 8–17. 83
- [142] Xu Nie et al. “A Kolsky torsion bar technique for characterization of dynamic shear response of soft materials.” In: *Experimental mechanics* 51.9 (2011), pp. 1527–1534. 83
- [143] Weinong W Chen and Bo Song. *Split Hopkinson (Kolsky) bar: design, testing and applications*. Springer Science & Business Media, 2010. 85

Appendix A

Background: Split-Hopkinson Pressure Bar

Dynamic compression experiments are used to probe the behavior of material under high rates of loading. In the context of this thesis, dynamic compression experiments refer to uniaxial compressive tests in which the strain rates range from 10^1 to 10^3 . During high velocity impact events, interaction between the projectile and the target can give rise to complex stress states within the target material. As a result, it is difficult to characterize the material response and tease out high rate properties from impact experiments alone.

In order to simplify the stress state and control the loading conditions, we employed a split-Hopkinson pressure bar (SHPB) for the high rate compression experiments in this study. The SHPB produces a nominally uniaxial compressive stress state and is commonly used to investigate the behavior of materials at strain rates ranging from 10^1 to 10^3 . This experimental setup has been used to study a range of different materials, including ceramics[4], foams[139], and metals[140]. It has also been modified to probe other stress states at dynamic strain rates, including tension[141] and shear[142]. Figure A.1) shows the SHPB apparatus used in this study.

An SHPB apparatus consists of a striker, an incident bar, and a transmitted bar. During an experiment, the test specimen is sandwiched between the incident and the transmitted bars. Using compressed air, the striker is launched at the incident bar to produce a compressive wave. This wave trav-

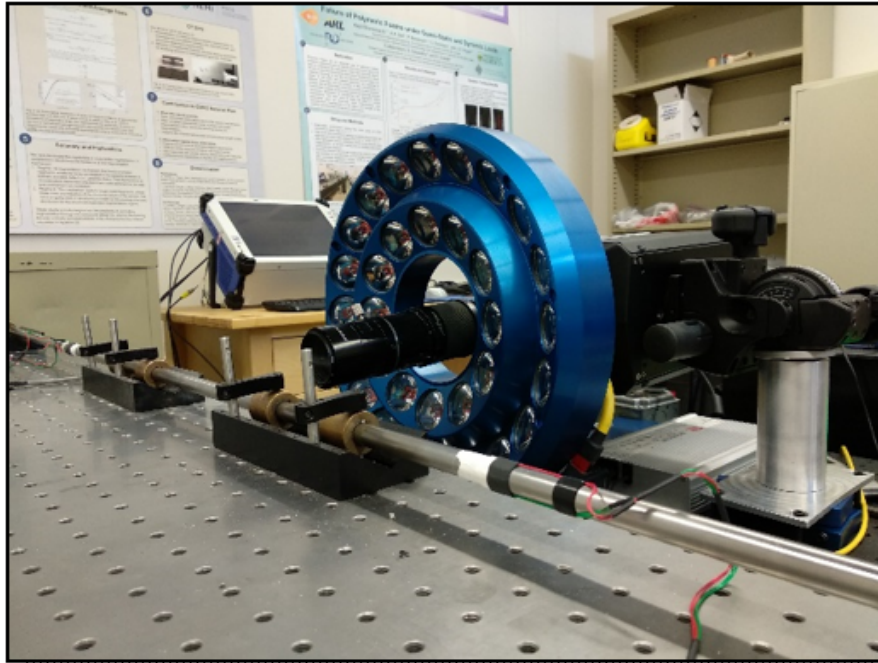


Figure A.1: Split-Hopkinson pressure bar setup: The incident and transmitted bars are shown in the foreground. The dynamic experiments were visualized using the Shimadzu HPV-X2 camera with the K2 DistaMax infinity lens and the REL Inc LED array ring light.

els down the incident bar and passes through the test specimen to produce the desired dynamic loading history. After passing through the specimen, the wave then travels through the transmitted bar. Using strain gauges mounted on the incident and transmitted bars, it is possible to record the compressive wave as it passes through the system. The strain gauges on the incident bar provides a measure of the compressive wave delivered by the striker. This is the wave profile that will load the specimen. The strain gauges on the transmitted bar provides a measure of the compressive wave that has passed through the specimen. This wave can be used to compute the stress history in the specimen.

By modifying the striker length, the pressure of the compressed air, and a pulse shaper, we are able to control the shape of the loading pulse and the loading rate. A pulse shaper is an object that is placed on the end of the incident bar facing the striker to attenuate the pulse imparted by the striker[143]. Depending on the size and material properties of the pulse shaper, different pulse shapes (e.g., triangular or top hat) can be achieved. In this thesis, we utilized a tin pulse shaper with a diameter of 3.175 mm and a thickness of 1 mm to generate a triangular loading pulse, which allowed us to probe strain rates of 60 to 130 s^{-1} in alumina.